

Measurement of nuclear effects in neutrino-argon interactions using generalized kinematic imbalance variables with the MicroBooNE detector

P. Abratenko,³⁸ O. Alterkait,³⁸ D. Andrade Aldana,¹⁵ L. Arellano,²¹ J. Asaadi,³⁷ A. Ashkenazi,³⁵ S. Balasubramanian,¹² B. Baller,¹² G. Barr,²⁸ D. Barrow,²⁸ J. Barrow,^{22,35} V. Basque,¹² O. Benevides Rodrigues,¹⁵ S. Berkman,^{12,24} A. Bhandari,²¹ A. Bhat,⁷ M. Bhattacharya,¹² M. Bishai,³ A. Blake,¹⁸ B. Bogart,²³ T. Bolton,¹⁷ J. Y. Book,¹⁴ M. B. Brunetti,⁴¹ L. Camilleri,¹⁰ Y. Cao,²¹ D. Caratelli,⁴ F. Cavanna,¹² G. Cerati,¹² A. Chappell,⁴¹ Y. Chen,³¹ J. M. Conrad,²² M. Convery,³¹ L. Cooper-Troendle,²⁹ J. I. Crespo-Anadón,⁶ R. Cross,⁴¹ M. Del Tutto,¹² S. R. Dennis,⁵ P. Detje,⁵ A. Devitt,¹⁸ R. Diurba,² Z. Djurcic,¹ R. Dorrill,¹⁵ K. Duffy,²⁸ S. Dytman,²⁹ B. Eberly,³³ P. Englezos,³⁰ A. Ereditato,^{7,12} J. J. Evans,²¹ R. Fine,¹⁹ O. G. Finnerud,²¹ W. Foreman,¹⁵ B. T. Fleming,⁷ N. Foppiani,¹⁴ D. Franco,⁷ A. P. Furmanski,²⁵ F. Gao,⁴ D. Garcia-Gamez,¹³ S. Gardiner,¹² G. Ge,¹⁰ S. Gollapinni,¹⁹ E. Gramellini,²¹ P. Green,²⁸ H. Greenlee,¹² L. Gu,¹⁸ W. Gu,³ R. Guenette,²¹ P. Guzowski,²¹ L. Hagaman,⁷ O. Hen,²² R. Hicks,¹⁹ C. Hilgenberg,²⁵ G. A. Horton-Smith,¹⁷ Z. Imani,³⁸ B. Irwin,²⁵ M. S. Ismail,²⁹ R. Itay,³¹ C. James,¹² X. Ji,^{26,3} J. H. Jo,³ R. A. Johnson,⁸ Y.-J. Jwa,¹⁰ D. Kalra,¹⁰ N. Kamp,²² G. Karagiorgi,¹⁰ W. Ketchum,¹² M. Kirby,¹² T. Kobilarcik,¹² I. Kreslo,² M. B. Leibovitch,⁴ I. Lepetic,³⁰ J.-Y. Li,¹¹ K. Li,⁴² Y. Li,³ K. Lin,³⁰ B. R. Littlejohn,¹⁵ H. Liu,³ W. C. Louis,¹⁹ X. Luo,⁴ C. Mariani,⁴⁰ D. Marsden,²¹ J. Marshall,⁴¹ N. Martinez,¹⁷ D. A. Martinez Caicedo,³² S. Martynenko,³ A. Mastbaum,³⁰ N. McConkey,³⁹ V. Meddage,¹⁷ J. Micallef,^{22,38} K. Miller,⁷ A. Mogan,⁹ T. Mohayai,^{12,16} M. Mooney,⁹ A. F. Moor,⁵ C. D. Moore,¹² L. Mora Lepin,²¹ M. M. Moudgalya,²¹ S. Mulleribabu,² D. Naples,²⁹ A. Navrer-Agasson,²¹ N. Nayak,³ M. Nebot-Guinot,¹¹ J. Nowak,¹⁸ N. Oza,¹⁰ O. Palamara,¹² N. Pallat,²⁵ V. Paolone,²⁹ A. Papadopoulou,¹ V. Papavassiliou,²⁷ H. B. Parkinson,¹¹ S. F. Pate,²⁷ N. Patel,¹⁸ Z. Pavlovic,¹² E. Piasetzky,³⁵ I. Pophale,¹⁸ X. Qian,³ J. L. Raaf,¹² V. Radeka,³ A. Rafique,¹ M. Reggiani-Guzzo,²¹ L. Ren,²⁷ L. Rochester,³¹ J. Rodriguez Rondon,³² M. Rosenberg,³⁸ M. Ross-Lonergan,¹⁹ C. Rudolf von Rohr,² I. Safa,¹⁰ G. Scanavini,⁴² D. W. Schmitz,⁷ A. Schukraft,¹² W. Seligman,¹⁰ M. H. Shaevitz,¹⁰ R. Sharankova,¹² J. Shi,⁵ E. L. Snider,¹² M. Soderberg,³⁴ S. Söldner-Rembold,²¹ J. Spitz,²³ M. Stancari,¹² J. St. John,¹² T. Strauss,¹² A. M. Szelc,¹¹ W. Tang,³⁶ N. Taniuchi,⁵ K. Terao,³¹ C. Thorpe,^{18,21} D. Torbunov,³ D. Totani,⁴ M. Touns,¹² Y.-T. Tsai,³¹ J. Tyler,¹⁷ M. A. Uchida,⁵ T. Usher,³¹ B. Viren,³ M. Weber,² H. Wei,²⁰ A. J. White,⁷ S. Wolbers,¹² T. Wongjirad,³⁸ M. Wospakrik,¹² K. Wresilo,⁵ W. Wu,^{12,29} E. Yandel,⁴ T. Yang,¹² L. E. Yates,¹² H. W. Yu,³ G. P. Zeller,¹² J. Zennaro,¹² and C. Zhang³

(The MicroBooNE Collaboration)*

¹Argonne National Laboratory (ANL), Lemont, IL, 60439, USA

²Universität Bern, Bern CH-3012, Switzerland

³Brookhaven National Laboratory (BNL), Upton, NY, 11973, USA

⁴University of California, Santa Barbara, CA, 93106, USA

⁵University of Cambridge, Cambridge CB3 0HE, United Kingdom

⁶Centro de Investigaciones Energéticas, Medioambientales y Tecnológicas (CIEMAT), Madrid E-28040, Spain

⁷University of Chicago, Chicago, IL, 60637, USA

⁸University of Cincinnati, Cincinnati, OH, 45221, USA

⁹Colorado State University, Fort Collins, CO, 80523, USA

¹⁰Columbia University, New York, NY, 10027, USA

¹¹University of Edinburgh, Edinburgh EH9 3FD, United Kingdom

¹²Fermi National Accelerator Laboratory (FNAL), Batavia, IL 60510, USA

¹³Universidad de Granada, Granada E-18071, Spain

¹⁴Harvard University, Cambridge, MA 02138, USA

¹⁵Illinois Institute of Technology (IIT), Chicago, IL 60616, USA

¹⁶Indiana University, Bloomington, IN 47405, USA

¹⁷Kansas State University (KSU), Manhattan, KS, 66506, USA

¹⁸Lancaster University, Lancaster LA1 4YW, United Kingdom

¹⁹Los Alamos National Laboratory (LANL), Los Alamos, NM, 87545, USA

²⁰Louisiana State University, Baton Rouge, LA, 70803, USA

²¹The University of Manchester, Manchester M13 9PL, United Kingdom

²²Massachusetts Institute of Technology (MIT), Cambridge, MA, 02139, USA

²³University of Michigan, Ann Arbor, MI, 48109, USA

²⁴Michigan State University, East Lansing, MI 48824, USA

²⁵University of Minnesota, Minneapolis, MN, 55455, USA

²⁶Nankai University, Nankai District, Tianjin 300071, China

²⁷New Mexico State University (NMSU), Las Cruces, NM, 88003, USA

²⁸University of Oxford, Oxford OX1 3RH, United Kingdom

²⁹University of Pittsburgh, Pittsburgh, PA, 15260, USA

³⁰*Rutgers University, Piscataway, NJ, 08854, USA*

³¹*SLAC National Accelerator Laboratory, Menlo Park, CA, 94025, USA*

³²*South Dakota School of Mines and Technology (SDSMT), Rapid City, SD, 57701, USA*

³³*University of Southern Maine, Portland, ME, 04104, USA*

³⁴*Syracuse University, Syracuse, NY, 13244, USA*

³⁵*Tel Aviv University, Tel Aviv, Israel, 69978*

³⁶*University of Tennessee, Knoxville, TN, 37996, USA*

³⁷*University of Texas, Arlington, TX, 76019, USA*

³⁸*Tufts University, Medford, MA, 02155, USA*

³⁹*University College London, London WC1E 6BT, United Kingdom*

⁴⁰*Center for Neutrino Physics, Virginia Tech, Blacksburg, VA, 24061, USA*

⁴¹*University of Warwick, Coventry CV4 7AL, United Kingdom*

⁴²*Wright Laboratory, Department of Physics, Yale University, New Haven, CT, 06520, USA*

We present a set of new generalized kinematic imbalance variables that can be measured in neutrino scattering. These variables extend previous measurements of kinematic imbalance on the transverse plane, and are more sensitive to modeling of nuclear effects. We demonstrate the enhanced power of these variables using simulation, and then use the MicroBooNE detector to measure them for the first time. We report flux-integrated single- and double-differential measurements of charged-current muon neutrino scattering on argon using a topology with one muon and one proton in the final state as a function of these novel kinematic imbalance variables. These measurements allow us to demonstrate that the treatment of charged current quasielastic interactions in GENIE version 2 is inadequate to describe data. Further, they reveal tensions with more modern generator predictions particularly in regions of phase space where final state interactions are important.

I. INTRODUCTION

All current and upcoming accelerator neutrino oscillation experiments rely on the precise modeling of neutrino-nucleus interactions to perform high-accuracy measurements [1–6]. The experimental sensitivity of these measurements can be limited by interaction modeling uncertainties related to nuclear effects [7, 8]. Significant progress has been made in understanding these effects and improving their modeling in neutrino event generators. Yet, outstanding tensions between measurement and theory still remain unresolved [9–11]. A major challenge in the study of neutrino-nucleus interactions originates from the wide-band accelerator neutrino beams, since nuclear effects cannot be easily disentangled when averaged over a broad energy spectrum. Examples of these are Fermi motion, final state interactions (FSI), and nucleon-nucleon correlations. However, it has been shown that kinematic imbalance variables in the plane transverse to the neutrino direction of travel are powerful tools that can be used to separate these nuclear effects, while minimizing the correlation to the neutrino energy [12].

In this work, we extend these measurements to generalized kinematic imbalance (GKI) variables by considering the longitudinal components along the beam direction. We illustrate with generator-level studies that these generalized variables achieve improved sensitivity to nuclear effects. Furthermore, we present the first flux-integrated single- and double-differential cross-section measurements for muon-neutrino charged-current (CC) reactions on argon (ν_μ -Ar) as a function of these generalized variables. Here we focus on reactions where a single muon-proton pair is reconstructed with no additional detected particles, similar to previous measurements [13, 14]. We refer to these events as CC1p0 π , and they are dominated by quasielastic (QE) interactions as it is required that there are no pions above the detection threshold. The results reported here use the MicroBooNE detector [15] with an exposure of 6.79×10^{20} protons on target from the Booster Neutrino Beam (BNB) [16] at Fermi National Accelerator Laboratory.

In Sec. II we define the GKI variables. Sec. III shows the enhanced sensitivity of GKI variables to nuclear effects by presenting comparisons to their transverse plane equivalents. In Sec. IV we present the first flux-integrated single- and double-differential cross section measurements in these variables using ν_μ -Ar CC1p0 π interactions recorded by the MicroBooNE detector. Finally, conclusions are presented in Sec. V.

* microboone_info@fnal.gov

II. OBSERVABLES

Variables based on the transverse kinematic imbalance are powerful discriminators between interaction models as reported by multiple experiments using a number of final states [12–14, 17–22]. The simplest case is for charged current quasielastic (CCQE) interactions, where the final state can be characterized by a muon with transverse momentum \vec{p}_T^μ and a proton with transverse momentum \vec{p}_T^p . To extend to other hadronic final states, the proton's momentum is replaced with the momentum of the combined hadronic system. In this work, however, we assume a final state containing only a muon and a proton. The kinematics of the two particle final state on the transverse plane can be fully characterized by a magnitude $\delta p_T = |\delta \vec{p}_T| = |\vec{p}_T^\mu + \vec{p}_T^p|$, as well as two angles,

$$\delta \phi_T = \cos^{-1} \left(\frac{-\vec{p}_T^\mu \cdot \vec{p}_T^p}{|\vec{p}_T^\mu| |\vec{p}_T^p|} \right), \quad (1)$$

$$\delta \alpha_T = \cos^{-1} \left(\frac{-\vec{p}_T^\mu \cdot \delta \vec{p}_T}{|\vec{p}_T^\mu| |\delta \vec{p}_T|} \right). \quad (2)$$

The muon transverse momentum (\vec{p}_T^μ) is equal and opposite to the transverse component of the momentum transfer to the nucleus (\vec{q}_T). The vector $\delta \vec{p}_T$ is the struck nucleon transverse momentum, and should be zero in the absence of initial state nucleon transverse momentum and FSI. Any non-zero value of $\delta \vec{p}_T$ can therefore be described as the missing transverse momentum (or rather, the negative thereof). Fermi motion inside the nucleus produces non-zero values of $\delta \vec{p}_T$ for QE interactions. However, more complex interactions, namely meson exchange currents (MEC), resonance interactions (RES) and deep inelastic scattering events (DIS), can still yield events with only a muon and a proton. This can be the case due to FSI, such as pion absorption, and such non-QE events populate the region above the Fermi momentum.

The variable $\delta \phi_T$ corresponds to the angle between the transverse momentum transfer vector and the final state transverse proton momentum (\vec{p}_T^p). These vectors would be aligned in the case of a free stationary nucleon target and this angle would be zero. Small values of $\delta \phi_T$ are produced by initial state motion, while larger values are indicative to FSI. The angle $\delta \alpha_T$ is defined between the transverse momentum transfer vector ($-\vec{p}_T^\mu$) and the transverse missing momentum vector ($\delta \vec{p}_T$). The angle is sensitive to FSI but much less sensitive to initial state nucleon motion. In the absence of FSI, $\delta \alpha_T$ does not have a preferred orientation and yields a fairly flat distribution. A representation of the kinematic imbalance variables on the transverse plane is shown in Fig. 1(a).

A more recent investigation identifies an alternative representation of the transverse missing momentum vector using the projection components perpendicular and parallel to the momentum transfer [19] [see Fig. 1(b)], given by

$$\delta p_{T,x} = (\hat{z} \times \hat{p}_T^\mu) \cdot \delta \vec{p}_T, \quad (3)$$

$$\delta p_{T,y} = -\hat{p}_T^\mu \cdot \delta \vec{p}_T. \quad (4)$$

These are the components of $\delta \vec{p}_T$ perpendicular and parallel, respectively, to the transverse momentum transfer vector.

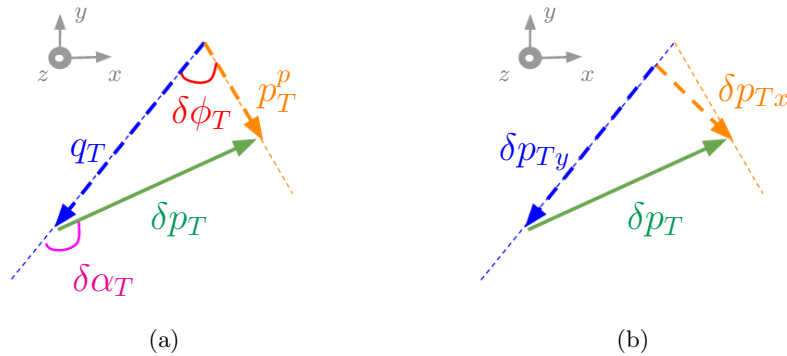


FIG. 1. (a) Representation of the kinematic imbalance variables on the transverse plane and (b) alternative representation using the projections parallel and perpendicular to the transverse momentum transfer vector. The finely dashed lines correspond to the direction of the momentum transfer (blue) and the proton (orange). The z axis corresponds to the neutrino direction of travel.

The interpretation of these variables on the transverse plane can be generalized to their three-dimensional equivalents. To do this, the longitudinal components of the missing momentum and momentum transfer vectors are required,

and therefore an assumption of the incoming neutrino energy has to be made. An initial attempt to perform this generalization is reported in Ref. [23] and first measured in Ref. [18], which assumes that a neutrino interacts via a CCQE interaction with a bound stationary neutron at rest inside a nucleus. This formalism was expanded to other final states in [24, 25]. This is then used to obtain an estimate for the neutrino energy and the three components of the missing momentum vector, labeled \vec{p}_n . Related studies that consider the longitudinal components are included in [21, 26].

We present a slightly different formalism which relies on conservation of energy and momentum. For the notation presented below, the speed of light c is assumed to be unity. For a massless neutrino, if the entire final state is visible, then the total visible energy and the longitudinal momentum will be the same. The “calorimetric visible energy” is constructed as the primary neutrino energy estimator

$$E_{\text{cal}} = E_\mu + K_p + B, \quad (5)$$

where E_μ is the total muon energy, K_p is the proton kinetic energy, and B the argon removal energy set to 30.9 MeV [27].

The second estimator of the neutrino energy is the total momentum along the neutrino direction of travel. This should be equal to the calorimetric energy if all final state particles have been observed and the target nucleon is at rest. Therefore the difference between the total longitudinal momentum and the calorimetric energy provides the longitudinal component of the missing momentum [28],

$$p_L = p_L^\mu + p_L^p - E_{\text{cal}}, \quad (6)$$

where $p_L^{\mu(p)}$ is the longitudinal component of the muon (proton) momentum vector. This definition of p_L is numerically very close to that in Ref. [23], but it enables a trivial generalization to other final states without having to make an assumption about the underlying interaction.

The missing momentum vector \vec{p}_n is obtained as the vector sum of the transverse missing momentum $\delta\vec{p}_T$ and the longitudinal component p_L . Under the assumption that FSI are weak or absent, the definitions given here produce a vector that aligns with the initial struck neutron momentum, consistent with the definitions used in previous work [23]. Assuming a neutrino traveling in the z direction of a detector coordinate system, the momentum transfer \vec{q} of the interaction is derived as the difference between the inferred neutrino and the muon momentum vectors

$$\vec{q} = E_{\text{cal}}\hat{z} - \vec{p}_\mu. \quad (7)$$

With these definitions, we generalize the transverse missing momentum variables to three dimensions [see Fig 2(a)] to be

$$p_n = |\vec{p}_n| = \sqrt{p_L^2 + \delta p_T^2}, \quad (8)$$

$$\phi_{3D} = \cos^{-1} \left(\frac{\vec{q} \cdot \vec{p}_p}{|\vec{q}| |\vec{p}_p|} \right), \quad (9)$$

$$\alpha_{3D} = \cos^{-1} \left(\frac{\vec{q} \cdot \vec{p}_n}{|\vec{q}| |\vec{p}_n|} \right). \quad (10)$$

The vector \vec{p}_n accounts for the missing momentum and is an estimate of the initial struck nucleon momentum when all the particles are reconstructed; ϕ_{3D} is the opening angle between the total momentum transfer vector \vec{q} and the proton momentum vector \vec{p}^p ; and α_{3D} is the angle between the momentum transfer vector \vec{q} and the missing momentum vector \vec{p}_n . These variables are the three-dimensional analogues to the ones on the transverse plane \vec{p}_T , $\delta\alpha_T$, and $\delta\phi_T$.

Likewise, the alternative representation on the transverse plane can also be extended to three dimensions [Fig. 2(b)], in the form

$$p_{n\perp,x} = (\hat{q}_T \times \hat{z}) \cdot \vec{p}_n, \quad (11)$$

$$p_{n\perp,y} = (\hat{q} \times (\hat{q}_T \times \hat{z})) \cdot \vec{p}_n, \quad (12)$$

$$p_{n\perp} = \sqrt{(p_{n\perp,x})^2 + (p_{n\perp,y})^2} = |p_n| \sin(\alpha_{3D}), \quad (13)$$

$$p_{n\parallel} = \hat{q} \cdot \vec{p}_n = |p_n| \cos(\alpha_{3D}). \quad (14)$$

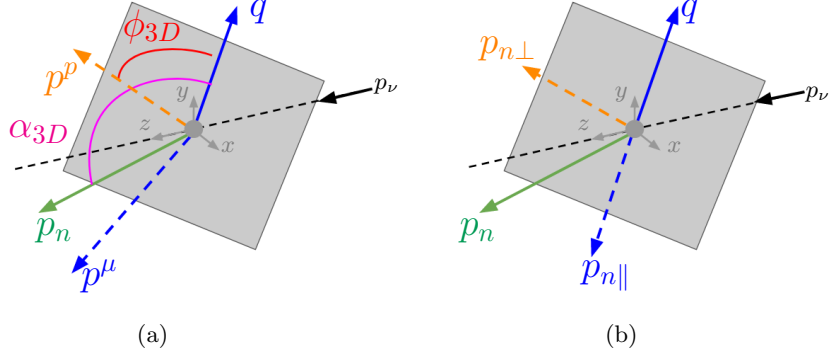


FIG. 2. (a) Representation of the generalized kinematic imbalance variables and (b) alternative representation using the projections parallel and perpendicular to the missing momentum vector. The z axis corresponds to the neutrino direction of travel.

Here, $p_{n\parallel}$ ($p_{n\perp}$) is the component of the missing momentum vector parallel (perpendicular) to the momentum transfer vector, $p_{n\perp,x}$ ($p_{n\perp,y}$) is the component of $p_{n\perp}$ in the neutrino-muon scattering plane (perpendicular to the neutrino-muon scattering plane), \hat{q} is the unit vector aligned with \vec{q} , \hat{q}_T is the unit vector aligned with the transverse component of \vec{q} , and \hat{z} is the unit vector aligned with the neutrino direction of travel (the z -axis).

These variables have been defined for a CCQE interaction with only a muon and a proton in the final state, however this is easily extended to other final states by summing the hadron momenta, and adjusting the assumed binding energy depending on the nucleon multiplicity. It is worth noting that Eqn. 10-14 are introduced for the first time in the literature.

III. GENERATOR COMPARISONS

To demonstrate the power of these novel variables, we use the CC1p0 π signal definition included in Refs. [13, 14] with several commonly-used neutrino interaction generators and model configurations, convoluted with the MicroBooNE ν_μ flux prediction [16]. The CC1p0 π signal definition used in this analysis includes all ν_μ -Ar scattering events with a final-state muon with momentum $0.1 < p_\mu < 1.2$ GeV/ c , and exactly one proton with $0.3 < p_p < 1$ GeV/ c . Events with final-state neutral pions at any momentum are excluded. Signal events may contain any number of protons below 300 MeV/ c or above 1 GeV/ c , neutrons at any momentum, and charged pions with momentum lower than 70 MeV/ c . A number of simulation predictions used for comparison correspond to GENIE model configurations, an event generator commonly used by Fermilab-based experiments. Our comparisons include an older GENIE version which was extensively used in the past, as well as more modern GENIE tunes currently used by MicroBooNE [13, 14, 29]. Additionally, comparisons to alternative event generators used by other neutrino experiments, such as T2K, or in the theory community, are included. Overflow (underflow) values are included in the last (first) bin. Table I lists a summary of the abbreviations of the generators and configurations used in this analysis, which are presented in more detail below. The relevant samples have been processed via the Nuisance framework [30].

TABLE I. Generators and configurations abbreviations used.

| Name | Generator / Configuration |
|-------|----------------------------------|
| Gv2 | GENIE v2.12.10 [31, 32] |
| G18 | GENIE v3.0.6 G18_10a_02_11a [33] |
| G18T | G18 with tune [29] |
| G21 | GENIE v3.2.0 G21_11b_00_000 [33] |
| GiBUU | GiBUU 2021 [34] |
| NuWro | NuWro v19.02.1 [35] |
| NEUT | NEUT v5.4.0 [36] |

The GENIE configurations used are:

- **GENIE v2.12.10 (Gv2)** [31, 32]: This version corresponds to a historical reference extensively used in the earliest MicroBooNE cross section analyses [37, 38] but superseded afterwards [29]. **Gv2** includes the Bodek-Ritchie Fermi Gas model, the Llewellyn Smith CCQE scattering prescription [39], the empirical MEC model [40], a Rein-Sehgal RES and coherent (COH) scattering model [41], the Bodek-Yang DIS model [42] coupled PYTHIA [43] for the hadronization part, and a data driven FSI model denoted as “hA” [44]. More modern **GENIE** versions include improvements over **Gv2** related to FSI issues, ground state modeling, and lepton-hadron correlations.
- **GENIE v3.0.6 G18_10a_02.11a (G18)** [33]: This more modern model configuration uses the local Fermi gas (LFG) model [45], the Nieves CCQE scattering prescription [46] which includes Coulomb corrections for the outgoing muon [47], and random phase approximation (RPA) corrections [48]. Additionally, it uses the Nieves MEC model [49], the Kuzmin-Lyubushkin-Naumov Berger-Sehgal RES [50, 51], Berger-Sehgal COH [52], and Bodek-Yang DIS [42] scattering models with the PYTHIA [43] hadronization part, and the hA2018 FSI model [53].
- **G18T** [29]: Corresponds to the same **G18** configuration with additional MicroBooNE-specific tuning.
- **GENIE v3.2.0 G21_11b_00.000 (G21)** [33]. This configuration includes the SuSAv2 prediction for the QE and MEC scattering modes [54] and the hN2018 FSI model [55]. The modeling options for RES, DIS, and COH interactions are the same as for **G18**.

The alternative event generator predictions are:

- **GiBUU 2021 (GiBUU)** [34]: Uses similar models to **GENIE**, but they are implemented in a coherent way by solving the Boltzmann-Uehling-Uhlenbeck transport equation [34]. The modeling includes the LFG model [45], a standard CCQE expression [56], an empirical MEC model, and a dedicated spin dependent resonance amplitude calculation following the MAID analysis [34]. The DIS model is from PYTHIA [43]. **GiBUU**’s FSI treatment propagates the hadrons through the residual nucleus in a nuclear potential consistent with the initial state.
- **NuWro v19.02.1 (NuWro)** [35]: Includes the LFG model [45], the Llewellyn Smith model for QE events [39], the Nieves model for MEC events [57], the Adler-Rarita-Schwinger formalism to calculate the Δ resonance explicitly [58], the BS COH [52] scattering model, an intranuclear cascade model for FSI [57], and a coupling to PYTHIA [43] for hadronization.
- **NEUT v5.4.0 (NEUT)** [59]: Corresponds to the combination of the LFG model [28, 45], the Nieves CCQE scattering prescription [46], the Nieves MEC model using a lookup table [49], the Berger Sehgal RES [50, 58, 60] and BS COH [52] scattering models, FSI with medium corrections for pions [31, 32], and PYTHIA [43] purposes.

If the interacting neutrino scatters off a stationary neutron and all final state particles are observed, p_n and δp_T become zero. Within the dense nuclear medium of a heavy nucleus like argon, these variables follow a broad distribution due to the struck nucleon motion before the interaction, with a high missing momentum tail from non-CCQE events. Figure 3 shows the p_n distribution for interaction types using **G18** and shows the corresponding breakdown for δp_T for the selected CC1p0 π events. Both results illustrate a CCQE dominance that is driven by the CC1p0 π signal definition. The non-CCQE events in the p_n distribution are concentrated at higher momentum values than in the δp_T distribution. Therefore, the missing momentum p_n illustrates enhanced discrimination capabilities between CCQE and non-CCQE events when compared to δp_T , as already demonstrated in Ref. [23].

To quantify this improved separation ability, we form signal acceptance-background rejection curves for both kinematic imbalance variables using **G18**, as shown in Fig. 4(a). Assuming events with a value of p_n less than a given “cut value” are retained, the fraction of true CCQE events accepted and the fraction of true non-CCQE events rejected can be calculated as a function of this cut value. An improved ability to isolate true CCQE events is observed for p_n compared to δp_T , while rejecting a larger fraction of non-CCQE background events. The evolution of the product between the signal acceptance and the background rejection denoted by “rejection \times acceptance” as a function of the cut value yields an optimal requirement at $p_n \approx 0.3$ GeV/c and at $\delta p_T \approx 0.2$ GeV/c [Fig. 4(b)]. The application of the corresponding selection criteria results in a CCQE loss of 25.3% for p_n and 29.7% for δp_T . The looser requirement on p_n results in a slightly more pure CCQE sample (95% CCQE purity) with higher statistics compared to the equivalent case with δp_T (92% CCQE purity). The same behavior is observed across all event generators and is shown in the Supplemental Material.

If a neutrino scatters off a moving, but unbound, neutron, α_{3D} becomes the angle of the struck nucleon direction before the interaction relative to the momentum transfer vector. There is no directional preference since the nucleus is at rest, so α_{3D} follows an approximately sinusoidal curve due to the phase space for a randomly distributed three-dimensional direction. However, FSI [55] in the nucleus introduce missing momentum, which is transferred from the hadronic system to the residual nucleus, reducing the magnitude of \vec{p}^p and enhancing the magnitude of the components transverse to \vec{q} . This effect enhances the contribution of events with higher values of α_{3D} . Like α_{3D} , the angular

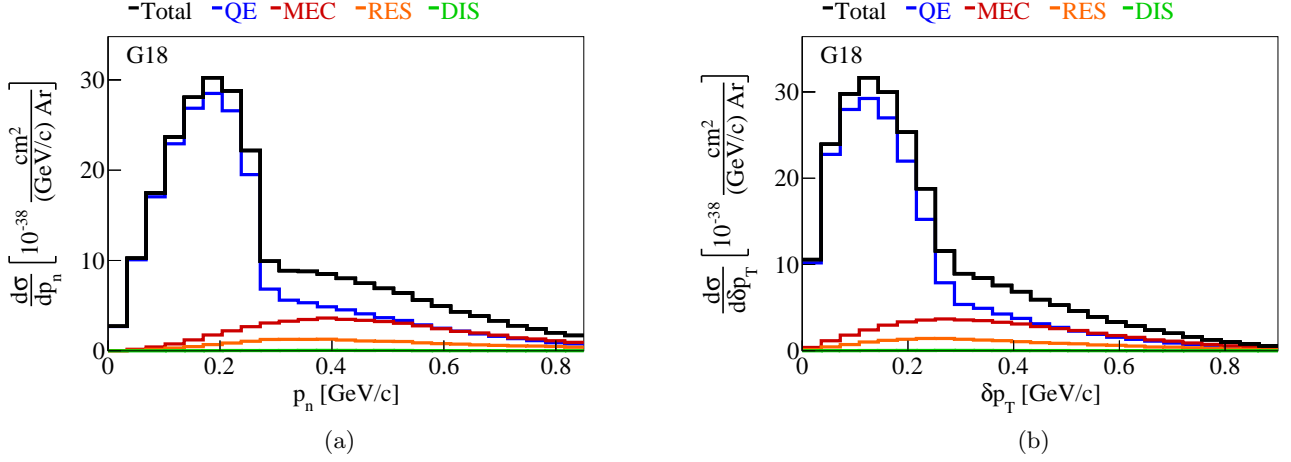


FIG. 3. The flux-integrated single-differential cross section interaction breakdown as a function of (a) p_n and (b) δp_T for the selected CC1p0 π events. Colored lines show the results of theoretical cross section calculations using the G18 prediction for QE (blue), MEC (red), RES (orange), and DIS (green) interactions.

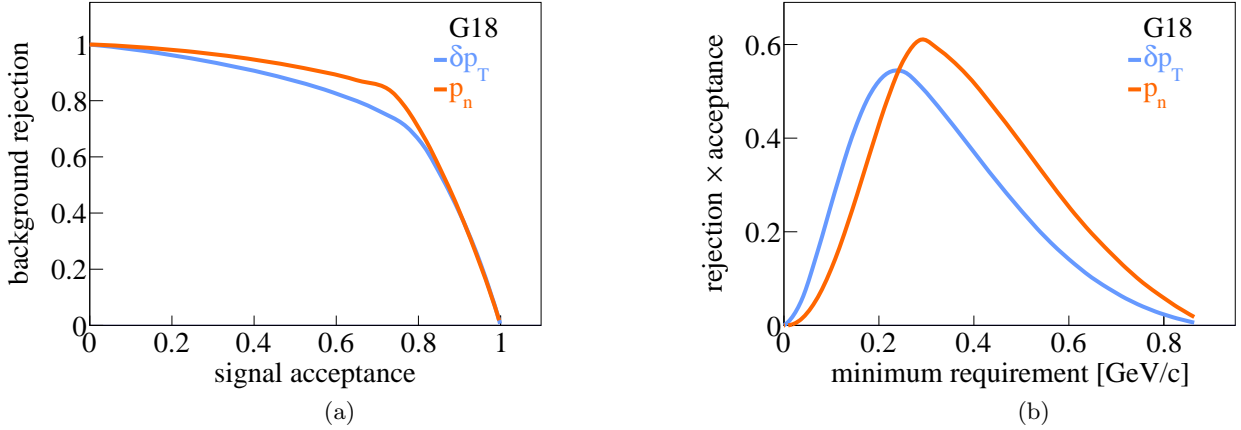


FIG. 4. (a) Signal acceptance fraction vs background rejection fraction as a function of the minimum requirement on either the missing momentum p_n (orange) or the transverse missing momentum δp_T (blue) for CC1p0 π events using the G18 prediction. (b) Evolution of the product between the signal acceptance and the background rejection denoted as “rejection \times acceptance” as a function of the minimum requirement.

orientation $\delta\alpha_T$ has been shown to be sensitive to FSI effects [12]. The distribution of $\delta\alpha_T$ illustrates a transition from a uniform angular orientation in the absence of FSI to one that peaks close to 180° due to the reduction of \vec{p}^p in the presence of FSI. Figure 5 shows the distribution of α_{3D} and $\delta\alpha_T$ for the G18 predictions with and without FSI, illustrating the impact of FSI on the shapes. Figure 6 shows the simulation predictions using several event generators for α_{3D} and $\delta\alpha_T$. The Gv2 model predicts a significantly different shape that peaks at the edges of the distribution. The GiBUU distribution is more sharply peaked in α_{3D} than the other generators and shows a larger discrepancy. All other event generators yield consistent predictions.

The third transverse kinematic imbalance variable, $\delta\phi_T$, has the benefit of not depending on the magnitude of the particles’ momenta, but only their direction. Therefore, it is often more precisely measured. The other two variables in the transverse plane rely on an accurate momentum reconstruction for the muon and the hadronic system. Unlike $\delta\phi_T$, the definition of ϕ_{3D} requires an estimation of the momentum transfer. Figure 7 shows the interactions using the G18 prediction for ϕ_{3D} with a turnover at low values. The corresponding $\delta\phi_T$ distribution monotonically decreases at higher values.

The ratios with and without FSI are shown in Fig. 8 for the stuck nucleon-missing momentum opening angles ($\delta\alpha_T$ or α_{3D}) and the proton-missing momentum opening angles ($\delta\phi_T$ or ϕ_{3D}) using several event generator predictions.

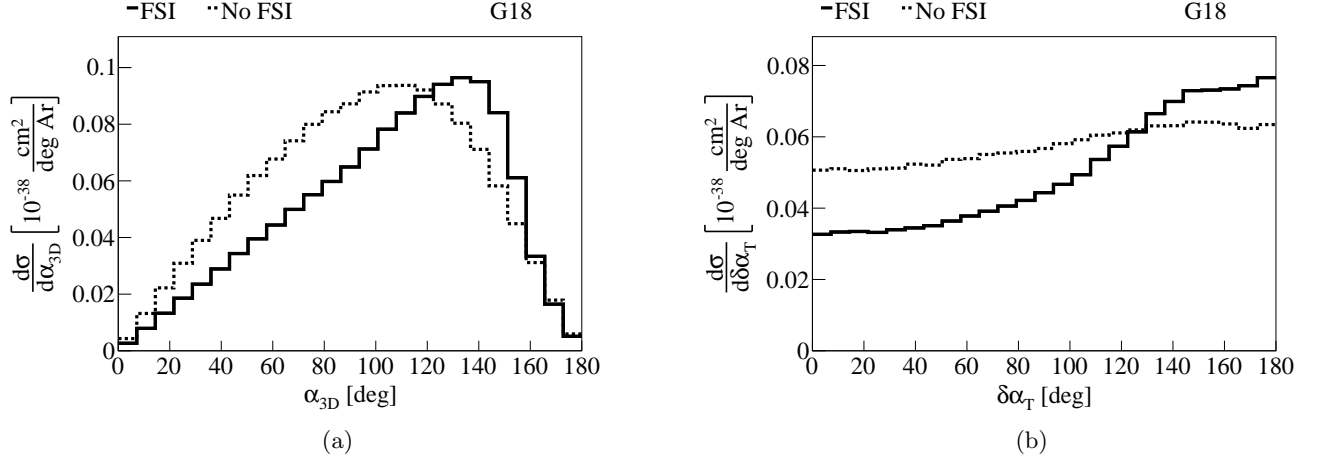


FIG. 5. Comparison of the flux-integrated single-differential cross section as a function of (a) α_{3D} and (b) $\delta\alpha_T$ with (solid) and without (dashed) FSI effects using the **G18** prediction for the selected CC1p0 π events.

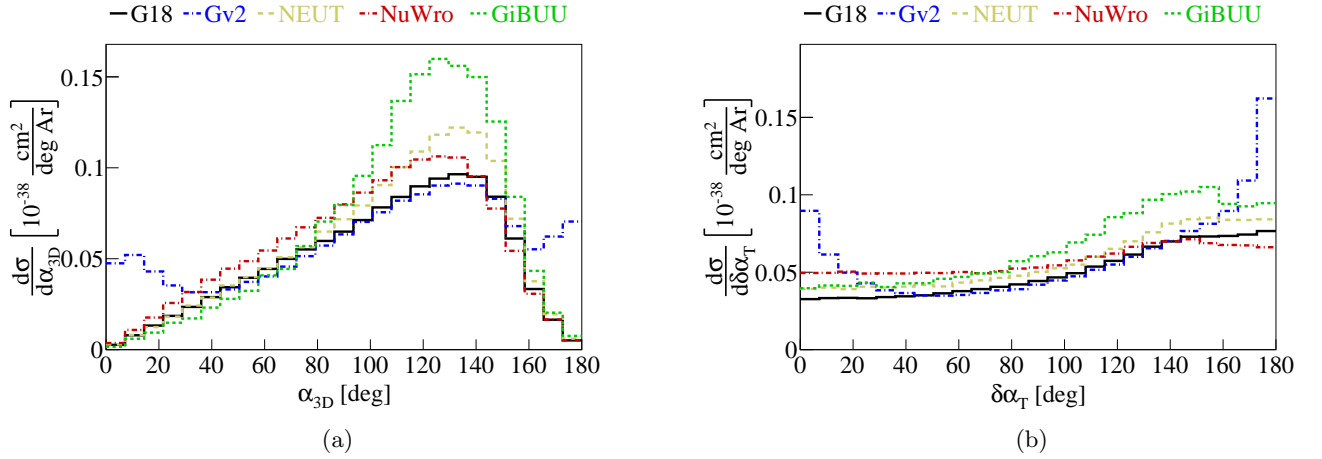


FIG. 6. The flux-integrated single-differential cross section as a function of (a) α_{3D} and (b) $\delta\alpha_T$ for the selected CC1p0 π events. Colored lines show the results of cross section calculations using the **G18** (solid black), **Gv2** (blue), **NEUT** (dashed pink), **NuWro** (red) and **GiBUU** (green) predictions.

Shape differences become more pronounced and yield a larger range of ratios when the GKI variables are used when compared to the equivalent TKI results, indicating greater sensitivity to the details of FSI modeling.

The projection variables $p_{n\parallel}$ and $p_{n\perp}$ vary when studied using several generators. Like its transverse equivalent, δp_{T_y} [14, 19], $p_{n\parallel}$ shows an asymmetric behavior due to the tendency for FSI to decelerate reinteracting hadrons [Fig. 9(a)]. In addition, **GiBUU** exhibits an offset by 0.15 GeV/c to smaller values, unlike any of the other event generators where the peak is centered around 0 GeV/c. The **GiBUU** interaction breakdown in Fig. 10(a) shows that the shift is driven both by the QE and MEC contributions. In the absence of FSI, the QE offset is no longer present and the asymmetric behavior is driven by the MEC contribution.

GiBUU shows a shift to higher values compared to the other generators for the $p_{n\perp}$ (Fig. 9). The **Gv2** distributions are significantly different compared to the other more modern generators, especially at lower values. In this older version, the hadronic and leptonic kinematics are generated independently which violates required correlations. This is modified for QE interactions in more recent versions (such as **G18**), resulting in smooth distributions that are similar to the other generators. The corresponding $p_{n\perp,x}$ and $p_{n\perp,y}$ distributions predict a much sharper peak around 0 GeV/c for **Gv2** compared to the other generators (Fig. 11). The results without FSI are presented in the Supplemental Material.

The two perpendicular projection variables, $p_{n\perp,x}$ and $p_{n\perp,y}$, show some shape differences which naively might not be expected. Due to the way these variables are defined, $p_{n\perp,y}$ is always perpendicular to the neutrino-muon

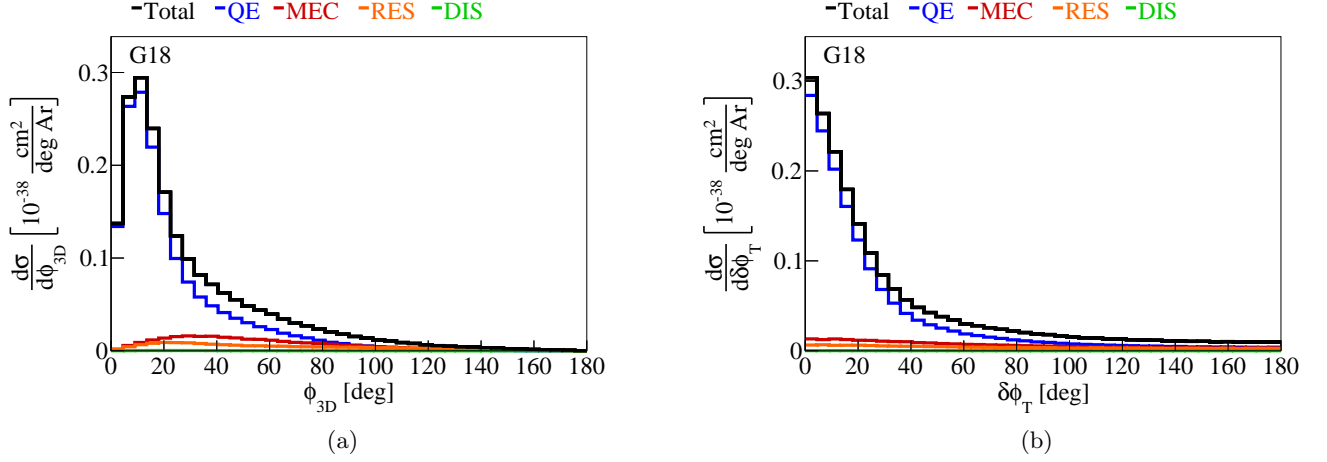


FIG. 7. The flux-integrated single-differential cross section interactions as a function of (a) ϕ_{3D} and (b) ϕ_T for the selected CC1p0 π events. Colored lines show the results of cross section calculations using the G18 prediction for QE (blue), MEC (red), RES (orange), and DIS (green) predictions.

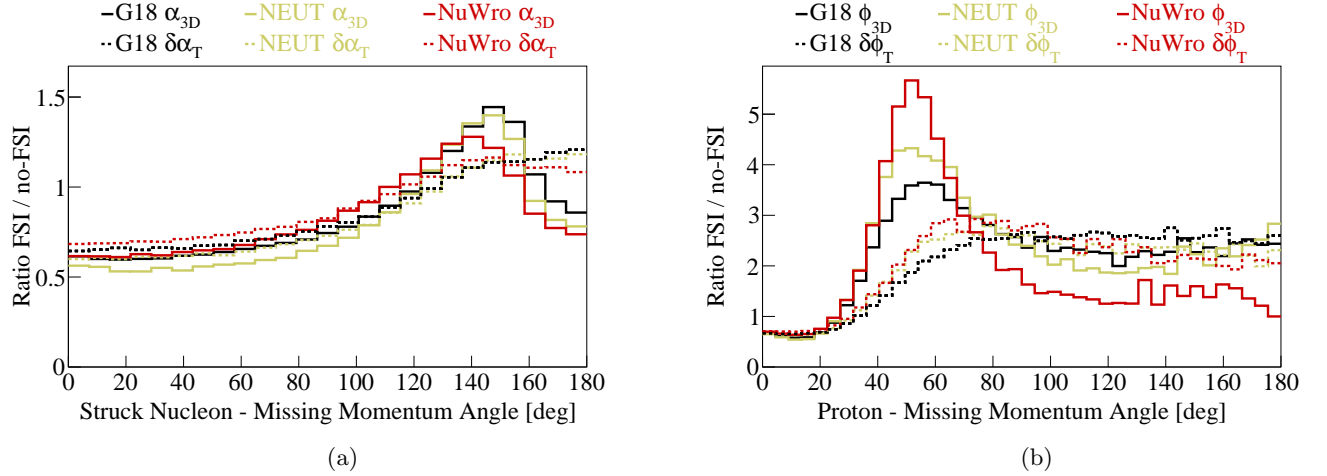


FIG. 8. Ratios with and without FSI for G18, NEUT, and NuWro predictions as a function of (a) the struck nucleon-missing momentum angle ($\delta\alpha_T$ or α_{3D}) and (b) the proton-missing momentum angle ($\delta\phi_T$ or ϕ_{3D}) for the selected CC1p0 π events.

scattering plane, which contains the vector \vec{q} . As there is no directional preference for nuclear motion, this is symmetric. Similarly, $p_{n\perp,x}$ is also perpendicular to \vec{q} , so naively it should also be symmetric. However, the variable is defined in the scattering plane. In this case missing energy can lead to small differences between the estimated direction of \vec{q} and the true momentum transfer vector. This leads to a slightly wider distribution with a tail at negative $p_{n\perp,x}$ values.

The sensitivity to nuclear effects of these variables becomes even more pronounced when performing double-differential measurements. As mentioned earlier, the angle α_{3D} is sensitive to FSI, with higher values of α_{3D} corresponding to events that primarily undergo FSI. The double-differential p_n cross section illustrates significant differences depending on whether FSI have been added or not (Fig. 12). For events with $\alpha_{3D} < 45^\circ$, FSI leads to a significant reduction in the normalization of the peak, while the high missing momentum tail is largely unaffected. Conversely, events with $135^\circ < \alpha_{3D} < 180^\circ$ yield a significantly enhanced high- p_n tail when FSI are included. That feature makes the high- α_{3D} region ideal to study the impact of FSI effects. We can study the FSI impact on p_n by isolating two groups of events, those with α_{3D} values $> 135^\circ$ and with $\alpha_{3D} < 45^\circ$. Figure 13(a) shows the QE-dominated low- α_{3D} region with a tail that vanishes at ≈ 0.5 GeV/c. The primary cause of the high- p_n tail in this region is interactions that produce additional undetected particles, and therefore consist mainly of non-QE interactions. Conversely, the high- α_{3D} region shown in Fig. 13(b) illustrates a much wider tail that extends up to ≈ 1 GeV/c. This tail has a significant contribution from MEC and RES events, as well as a large population of events from QE

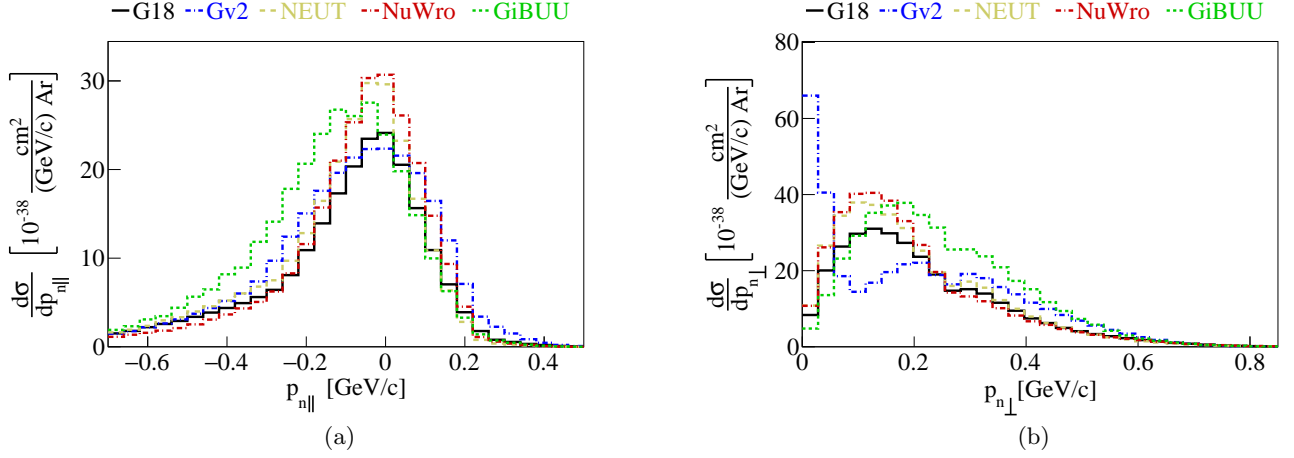


FIG. 9. The flux-integrated single-differential cross section as a function of (a) $p_{n\parallel}$ and (b) $p_{n\perp}$ for the selected CC1p0 π events. Colored lines show the results of cross section calculations using the G18 (solid black), Gv2 (blue), NEUT (dashed pink), NuWro (red) and GiBUU (green) generators.

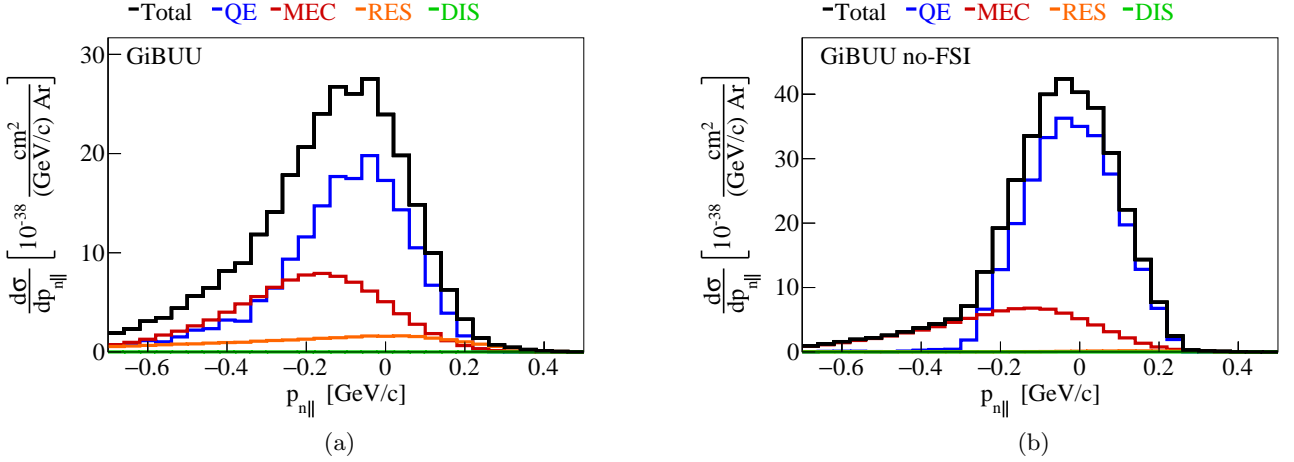


FIG. 10. The flux-integrated single-differential cross section interaction breakdown as a function of $p_{n\parallel}$ (a) with FSI and (b) without FSI for the selected CC1p0 π events. Colored lines show the results of cross section calculations using the GiBUU prediction for QE (blue), MEC (red), RES (orange), and DIS (green) generators.

interactions that undergo FSI and therefore yield higher p_n values.

A complementary way to group the selected events is by missing momentum ($p_n < 0.2$ GeV/c and $p_n > 0.4$ GeV/c). The double-differential cross section in α_{3D} yields a distribution that approximately follows the expected sine-curve behavior when events with low missing momentum are used [Fig. 14(a)]. The same shape is observed when FSI are turned off [Fig. 15(a)]. A different shape is observed in Fig. 14(b) for events with high missing momentum with a pronounced peak at high α_{3D} values, which is driven by QE events. On the other hand, MEC and RES events result in a wider range of α_{3D} angles and less peaked distributions, illustrating that the missing momentum has less directional preference. Furthermore, the region where $\alpha_{3D} < 90^\circ$ is dominated by MEC events across all event generators due to the missing momentum introduced by undetected particles. The prediction without FSI yields a smoother distribution [Fig. 15(b)].

IV. MICROBOONE CROSS SECTION MEASUREMENT

To perform the first measurement of the cross section as a function of these variables, we use three years of data collected by the MicroBooNE detector. MicroBooNE is an 85-tonne active mass liquid argon time projection chamber

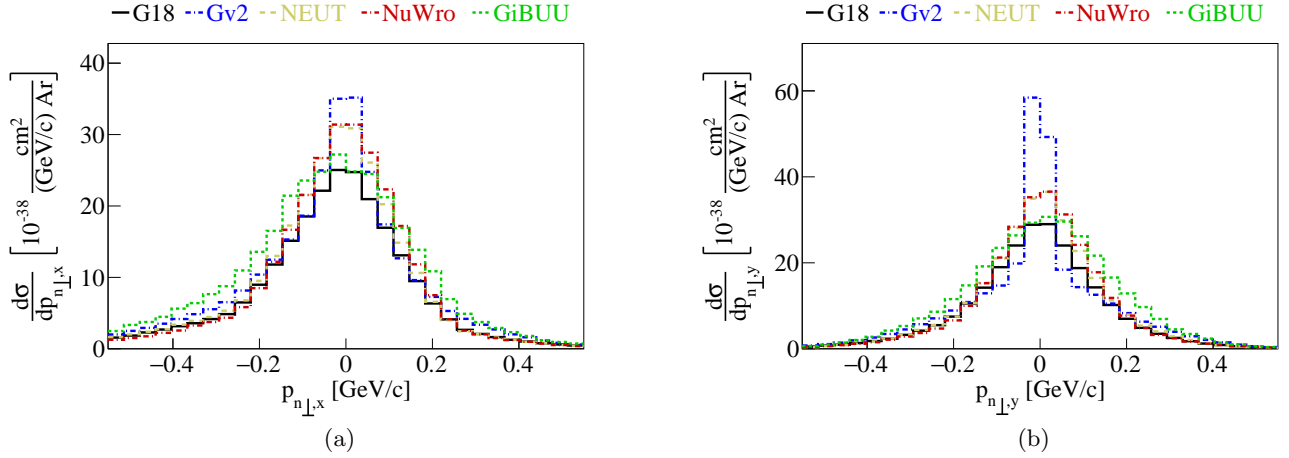


FIG. 11. The flux-integrated single-differential cross section as a function of (a) $p_{n\perp,x}$ and (b) $p_{n\perp,y}$ for the selected CC1p0 π events. Colored lines show the results of cross section calculations using the G18 (solid black), Gv2 (blue), NEUT (dashed pink), NuWro (red) and GiBUU (green) generators.

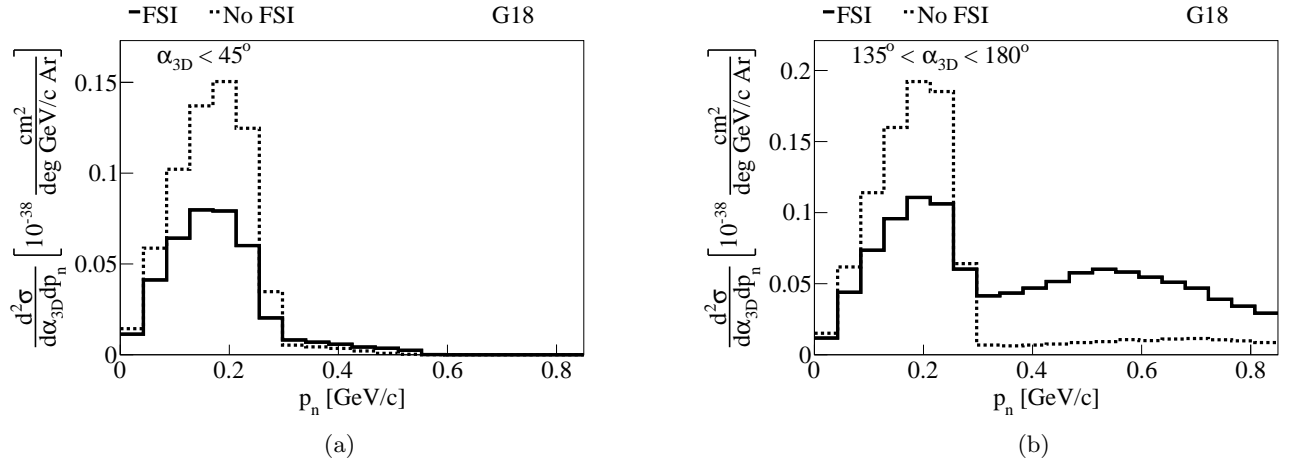


FIG. 12. Comparison of the flux-integrated double-differential cross section as a function of p_n for (a) $\alpha_{3D} < 45^\circ$ and (b) $135^\circ < \alpha_{3D} < 180^\circ$ with (solid) and without (dashed) FSI effects using the G18 prediction for the selected CC1p0 π events.

in the Booster Neutrino Beam (BNB). The MicroBooNE detector is described in detail in Ref. [15]. We use the same event selection and measurement strategy as used in Refs. [13, 14], and the same CC1p0 π definition for the variables of interest as described in Sec. II.

Data are processed by filtering noise and deconvolving the wire response to produce unipolar signals, which are then fitted with Gaussian functions to produce hits. The Pandora multi-algorithm pattern recognition package [61] is used to cluster hits, match them across wire planes, and construct tracks and showers. Topological and optical information are used to identify and remove cosmic tracks. The remaining tracks and showers are grouped into neutrino candidates. Events are selected by requiring a neutrino candidate with exactly two reconstructed tracks by applying particle identification requirements based on dE/dx measurements to ensure the tracks are muon-like or proton-like, respectively. More details on the selection can be found in Ref. [14].

Uncertainties related to the incident neutrino flux [16], interaction model [29], particle propagation [62], and detector response [63] are assessed separately to produce a covariance matrix describing the uncertainty of the predicted event rate. The binning is chosen to balance resolution and statistics. The Wiener-Singular Value Decomposition unfolding technique [64] is used to transform both the data measurement and covariance matrix into a regularized phase space. The technique requires the construction of a response matrix describing the expected detector smearing and reconstruction efficiency, for which it corrects. The unfolding is performed for each one of the observables of interest using the G18T model. Each measurement is accompanied by an output additional smearing matrix A_C which performs

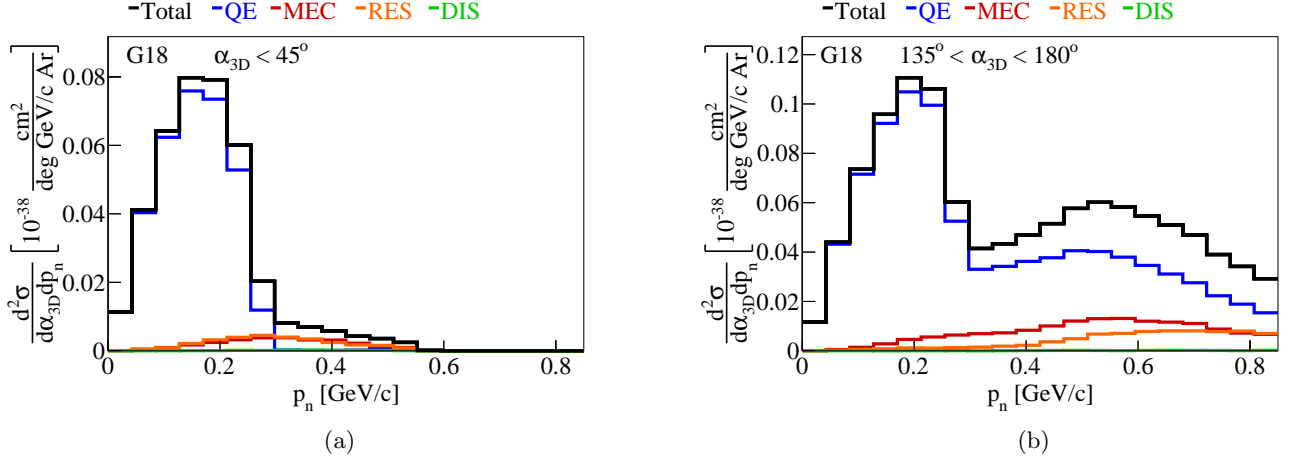


FIG. 13. The flux-integrated double-differential cross section interaction breakdown as a function of $p_{n\parallel}$ for (a) $\alpha_{3D} < 45^\circ$ and (b) $135^\circ < \alpha_{3D} < 180^\circ$ for the selected CC1p0 π events. Colored lines show the results of theoretical cross section calculations using the G18 prediction for QE (blue), MEC (red), RES (orange), and DIS (green) interactions.

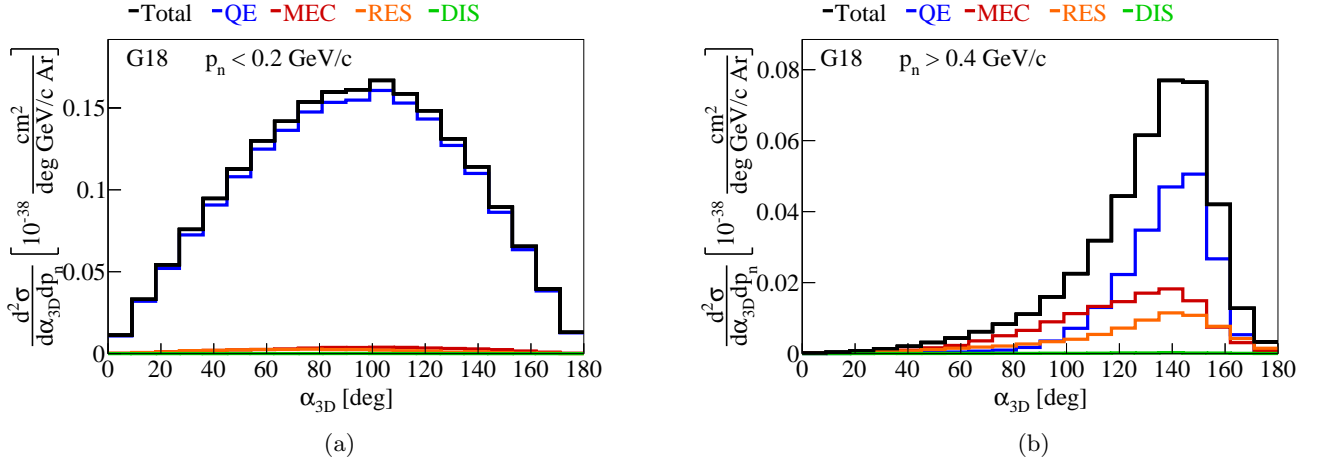


FIG. 14. The flux-integrated double-differential cross sections as a function of α_{3D} for (a) $p_n < 0.2 \text{ GeV/c}$ and (b) $p_n > 0.4 \text{ GeV/c}$ for the selected CC1p0 π events. Colored lines show the results of cross section calculations using the G18 prediction for QE (blue), MEC (red), RES (orange), and DIS (green) predictions.

the conversion from the true to the regularized phase space. The A_C matrix is included in the Supplemental Material and needs to be applied to all theory predictions in order to compare to the data measurements, even though its effect is small.

The robustness of the unfolding method was tested using fake data studies with alternative generator predictions, which are presented in the Supplemental Material. Namely, we investigated three fake data samples: (a) using NuWro events, (b) by removing the weights corresponding to the MicroBooNE tune and, (c) by multiplying the weight for the MEC events by a factor of two. We then extracted the cross section from these fake data using our nominal MC response matrices, as well as the Wiener-SVD filter when only the covariances related to the relevant uncertainties were included. We found that the combination of these uncertainties covered the difference between the unfolded fake data prediction and the corresponding alternative-generator theory prediction. Additionally, the aforementioned comparisons yielded χ^2/ndof values below unity and p-values close to 1, further supporting the robustness of our unfolding procedure.

The unfolded event rate has the predicted background subtracted before the unfolding. It is further divided by the integrated neutrino flux and number of argon nuclei in the fiducial volume to report a differential cross section. In the results presented below, the inner error bars on the cross sections correspond to the data statistical uncertainties. The systematic uncertainties are decomposed into data shape- and normalization-related sources following the procedure

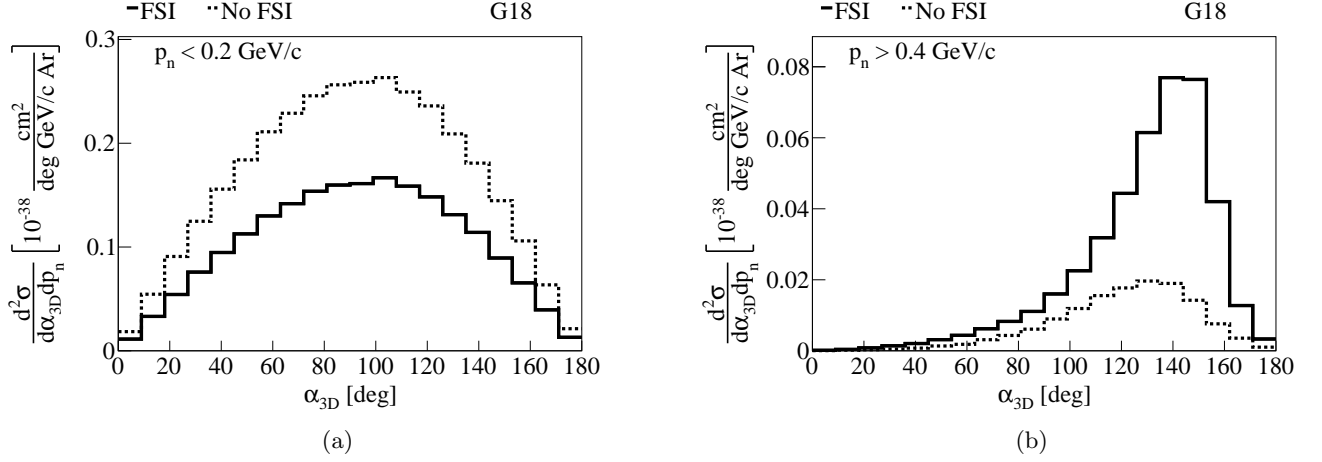


FIG. 15. The flux-integrated double-differential cross sections as a function of α_{3D} for (a) $p_n < 0.2 \text{ GeV/c}$ and (b) $p_n > 0.4 \text{ GeV/c}$ with (solid) and without (dashed) FSI effects using the G18 prediction for the selected CC1p0 π events.

outlined in Ref. [65]. The cross-term uncertainties are incorporated in the normalization. The outer error bars on the reported cross sections correspond to data statistical and shape uncertainties added in quadrature. The data normalization uncertainties are presented as a band at the bottom of each plot. Overflow (underflow) values are included in the last (first) bin. The degrees of freedom correspond to the number of bins. The χ^2/ndf data comparison for each generator shown on all the figures takes into account the total covariance matrix. More details on the systematic uncertainties and the cross-section extraction technique can be found in Ref. [14].

Figures 16-18 show the single-differential cross sections as a function of the p_n , α_{3D} , and ϕ_{3D} compared to several predictions. We conclude that Gv2 is a poor description of the data and results in large χ^2 values. Among the other generator predictions, GiBUU provides the best description of the data in α_{3D} . There is a spread in p_n and ϕ_{3D} with G21 describing the data best. Unlike these variables, G21 shows a poor agreement with the data in α_{3D} . G18T illustrates a similar pattern as G21 with a better agreement in p_n and ϕ_{3D} and a worse performance in α_{3D} .

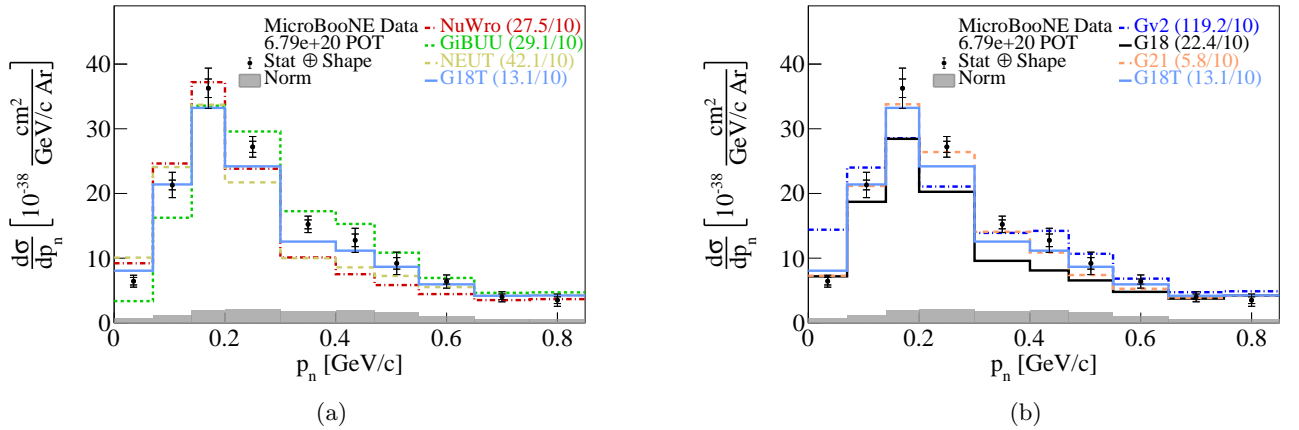


FIG. 16. The flux-integrated single-differential cross sections as a function of p_n with (a) generator and (b) GENIE configuration predictions compared to data. Inner and outer error bars show the statistical and total (statistical and shape systematic) uncertainty at the 1σ , or 68%, confidence level. The gray band shows the normalization systematic uncertainty. The numbers in parentheses give the χ^2/ndf calculation for each one of the predictions.

The different projections of p_n parallel and perpendicular to the momentum transfer are shown in Figs. 19 - 22. Again Gv2 provides a poor description of the data, particularly in the case of $p_{n\perp}$. The data show a large tail at negative values of $p_{n\parallel}$ as expected from the effects of FSI. The predictions in this region show large variation due to the different ways of modeling FSI. Based on the χ^2/ndf , GiBUU provides the best description of this data in most

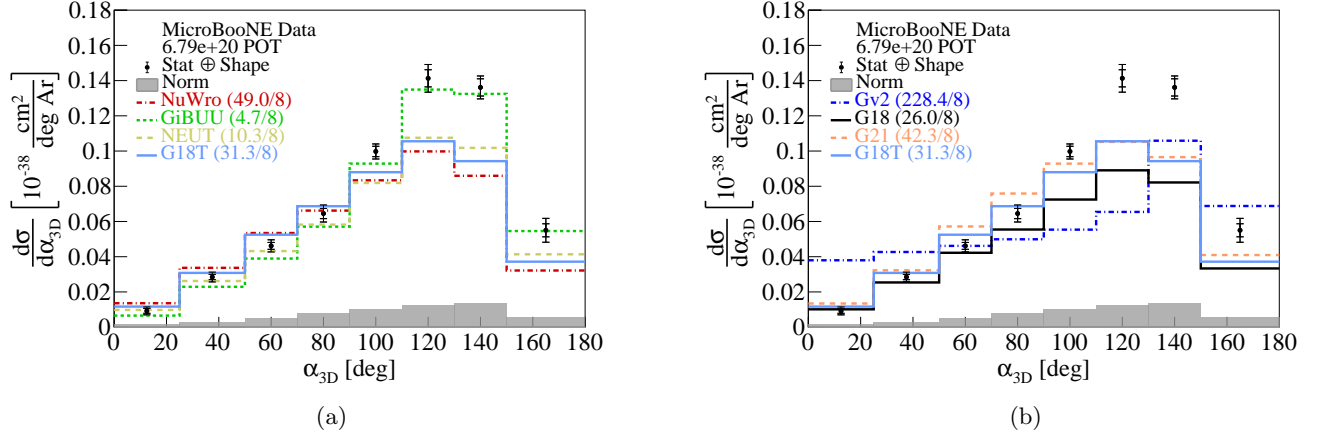


FIG. 17. The flux-integrated single-differential cross sections as a function of α_{3D} with (a) generator and (b) GENIE configuration predictions compared to data. Inner and outer error bars show the statistical and total (statistical and shape systematic) uncertainty at the 1σ , or 68%, confidence level. The gray band shows the normalization systematic uncertainty. The numbers in parentheses give the χ^2/ndf calculation for each one of the predictions.

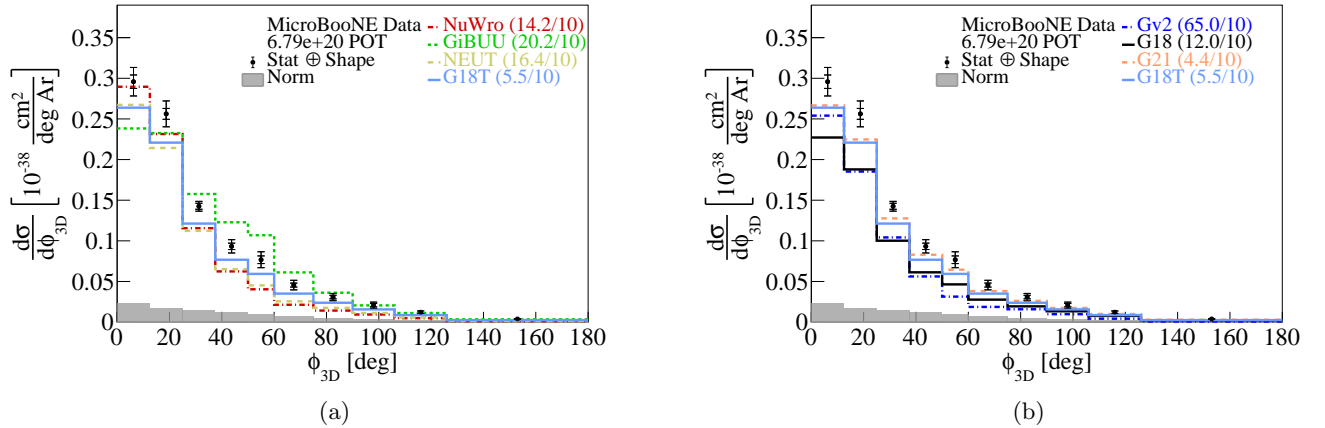


FIG. 18. The flux-integrated single-differential cross sections as a function of ϕ_{3D} with (a) generator and (b) GENIE configuration predictions compared to data. Inner and outer error bars show the statistical and total (statistical and shape systematic) uncertainty at the 1σ , or 68%, confidence level. The gray band shows the normalization systematic uncertainty. The numbers in parentheses give the χ^2/ndf calculation for each one of the predictions.

variables. G18T provides the best performance in the case of p_\perp and $p_{\perp,x}$. Conversely, there is a spread in performance among the generators in the description of $p_{\perp,y}$ with G21 yielding the lowest χ^2/ndf ratio.

As discussed in Sec. III, the sensitivity of the generalized kinematic imbalance variables can be further enhanced when performing multi-differential measurements. Following the approach outlined in Refs. [13, 14], we present double-differential measurements as a function of p_n and α_{3D} .

FSI effects are minimal for the double-differential cross section of p_n with $\alpha_{3D} < 45^\circ$ and, as expected, the tail of the p_n distribution is significantly suppressed (Fig. 23). The χ^2/ndf is reasonably consistent across all event generators apart from Gv2. This observation could be driven by the fact that the more modern CCQE models used by GENIE v3 and alternative event generators are very similar. This improved picture originates from the fairly well-understood QE interaction channel that has been extensively investigated. Conversely, the region $\alpha_{3D} > 135^\circ$ (Fig. 24) contains a large fraction of events that undergo FSI, leading to an enhanced high- p_n tail, which is under-predicted by most generators. Furthermore, GiBUU shows an offset to the right compared to other event generators and demonstrates the best agreement with the data.

Figures 25 and 26 show the double-differential measurement in α_{3D} for events with low and high values of p_n ,

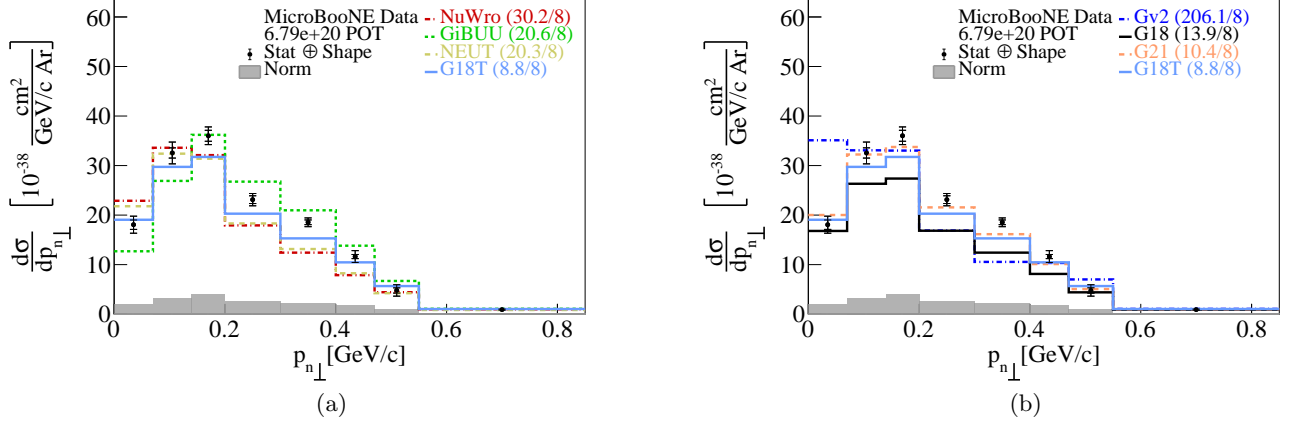


FIG. 19. The flux-integrated single-differential cross sections as a function of $p_{n\perp}$ with (a) generator and (b) GENIE configuration predictions compared to data. Inner and outer error bars show the statistical and total (statistical and shape systematic) uncertainty at the 1σ , or 68%, confidence level. The gray band shows the normalization systematic uncertainty. The numbers in parentheses give the χ^2/ndf calculation for each one of the predictions.

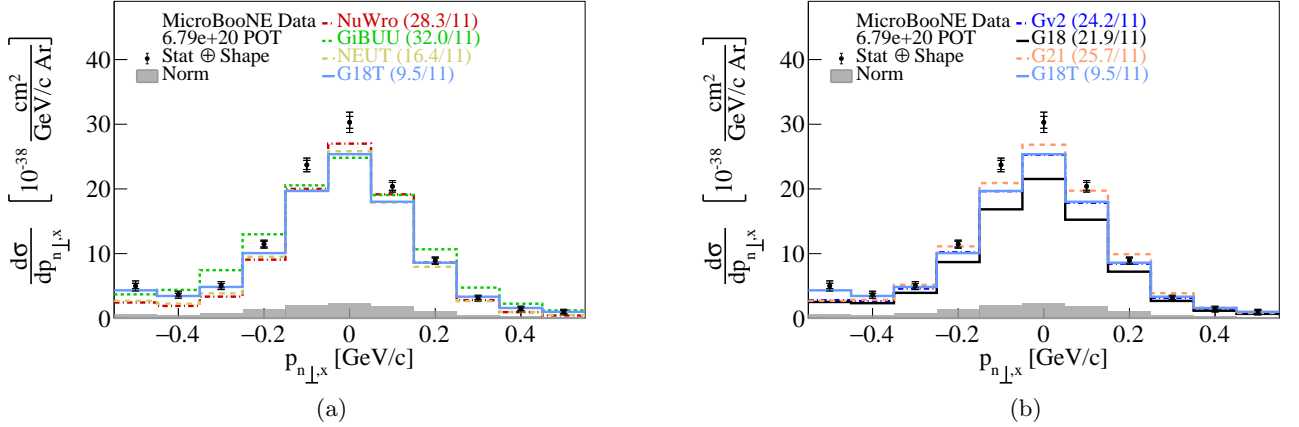


FIG. 20. The flux-integrated single-differential cross sections as a function of $p_{n\perp,x}$ with (a) generator and (b) GENIE configuration predictions compared to data. Inner and outer error bars show the statistical and total (statistical and shape systematic) uncertainty at the 1σ , or 68%, confidence level. The gray band shows the normalization systematic uncertainty. The numbers in parentheses give the χ^2/ndf calculation for each one of the predictions.

respectively. For events with low missing momentum, the distribution is very symmetric and approximately follows the $\sin(\alpha_{3D})$ shape as expected. FSI predominantly remove events from this region of phase space, leading to normalization differences between generators, with the exception of Gv2 which illustrates a significantly different behavior. Conversely, events with high missing momentum (Fig. 26) show a large asymmetry with strong enhancement in the FSI-driven region at high values of α_{3D} . Apart from Gv2, all generator predictions show similar shapes with some normalization differences. Gv2 predicts an enhanced tail at low values of α_{3D} which does not appear in the data. This low- α_{3D} , high- p_n region contains a large contribution ($\geq 50\%$) from MEC according to generator predictions. Most models provide a reasonable description of the data in this region.

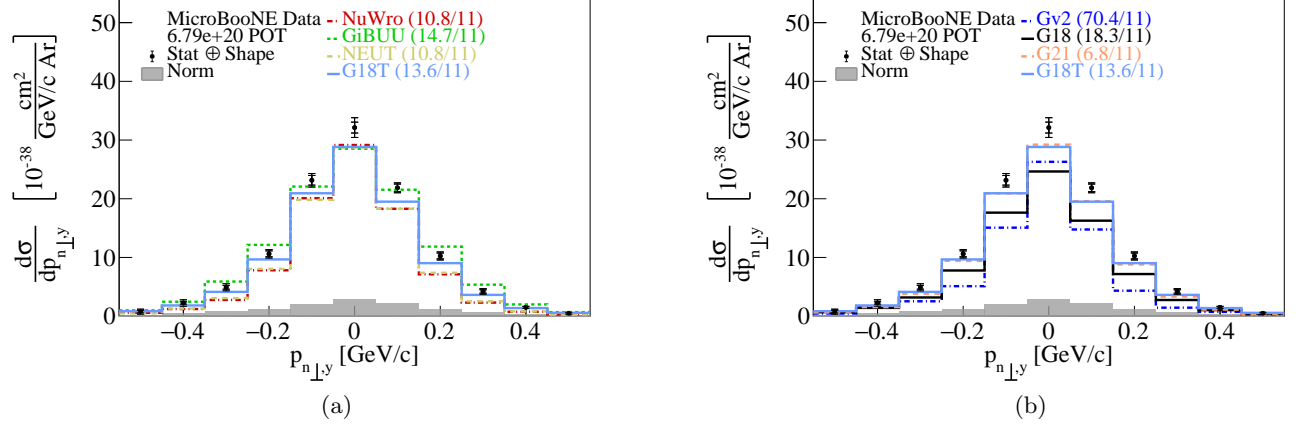


FIG. 21. The flux-integrated single-differential cross sections as a function of $p_{n\perp,y}$ with (a) Generator and (b) GENIE configuration predictions compared to data. Inner and outer error bars show the statistical and total (statistical and shape systematic) uncertainty at the 1 σ , or 68%, confidence level. The gray band shows the normalization systematic uncertainty. The numbers in parentheses give the χ^2/ndf calculation for each one of the predictions.

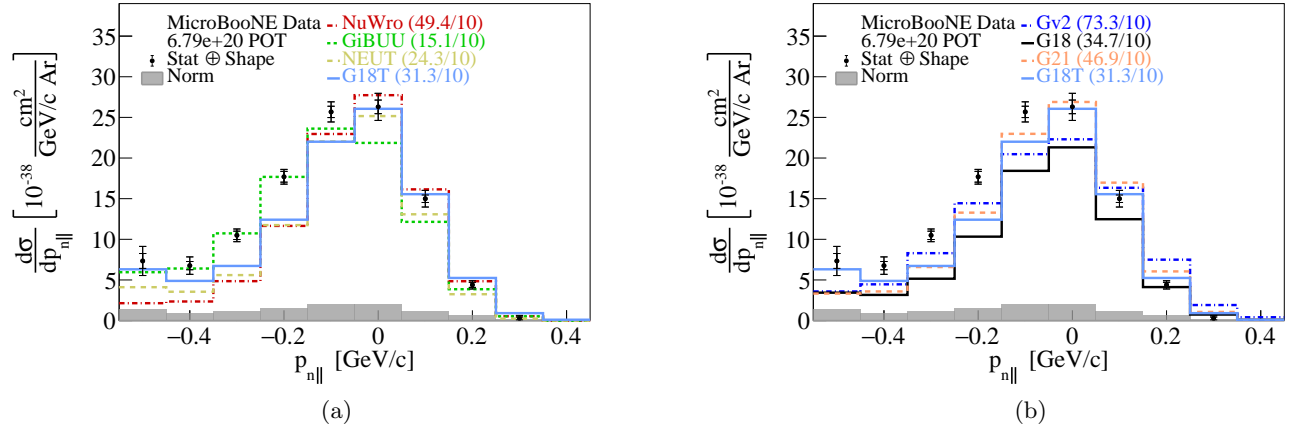


FIG. 22. The flux-integrated single-differential cross sections as a function of $p_{n\parallel}$ with (a) Generator and (b) GENIE configuration predictions compared to data. Inner and outer error bars show the statistical and total (statistical and shape systematic) uncertainty at the 1 σ , or 68%, confidence level. The gray band shows the normalization systematic uncertainty. The numbers in parentheses give the χ^2/ndf calculation for each one of the predictions.

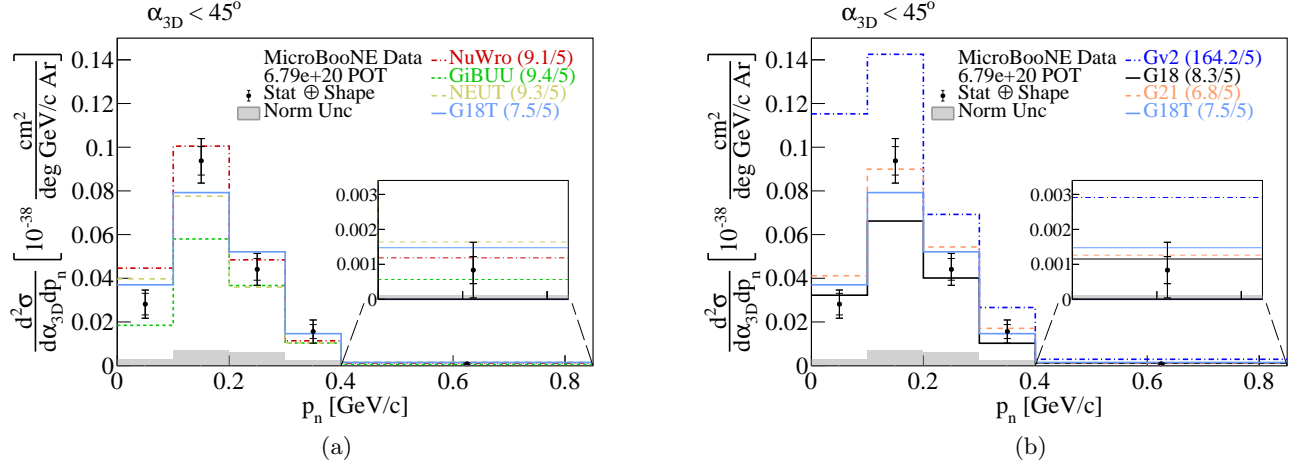


FIG. 23. The flux-integrated double-differential cross sections as a function of p_n for $\alpha_{3D} < 45^\circ$ with (a) generator and (b) GENIE configuration predictions compared to data. Inner and outer error bars show the statistical and total (statistical and shape systematic) uncertainty at the 1σ , or 68%, confidence level. The gray band shows the normalization systematic uncertainty. The numbers in parentheses give the χ^2/ndf calculation for each one of the predictions.

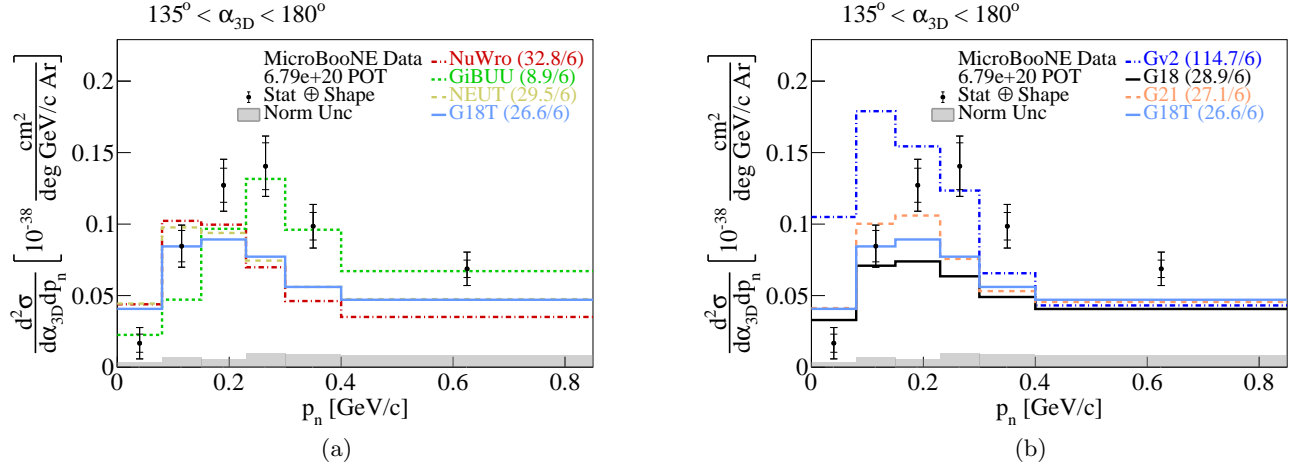


FIG. 24. The flux-integrated double-differential cross sections as a function of $135^\circ < \alpha_{3D} < 180^\circ$ with (a) Generator and (b) GENIE configuration predictions compared to data. Inner and outer error bars show the statistical and total (statistical and shape systematic) uncertainty at the 1σ , or 68%, confidence level. The gray band shows the normalization systematic uncertainty. The numbers in parentheses give the χ^2/ndf calculation for each one of the predictions.

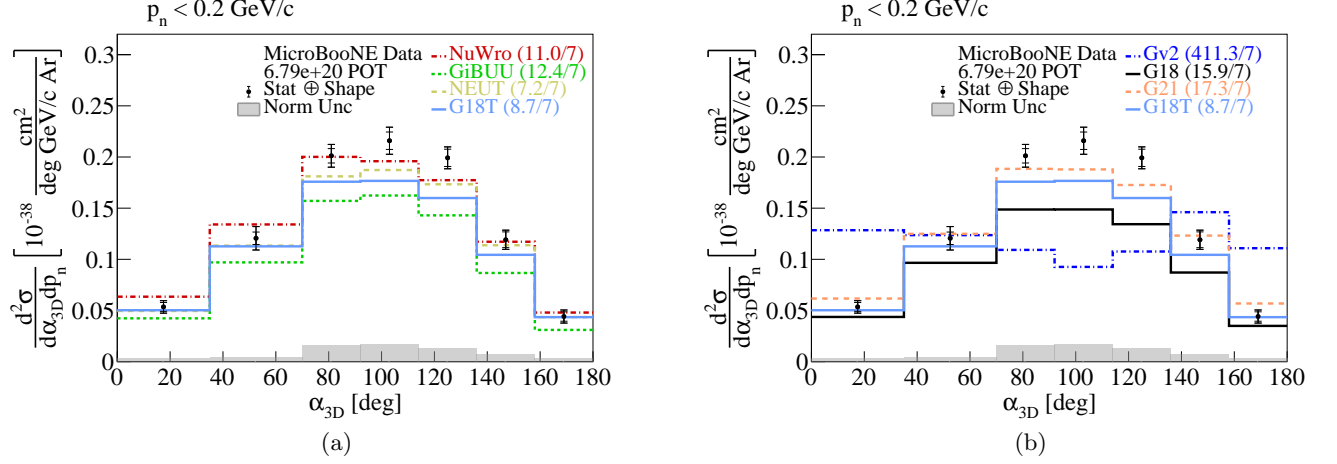


FIG. 25. The flux-integrated double-differential cross sections as a function of α_{3D} for $p_n < 0.2$ GeV/c with (a) generator and (b) GENIE configuration predictions compared to data. Inner and outer error bars show the statistical and total (statistical and shape systematic) uncertainty at the 1σ , or 68%, confidence level. The gray band shows the normalization systematic uncertainty. The numbers in parentheses give the χ^2/ndf calculation for each one of the predictions.

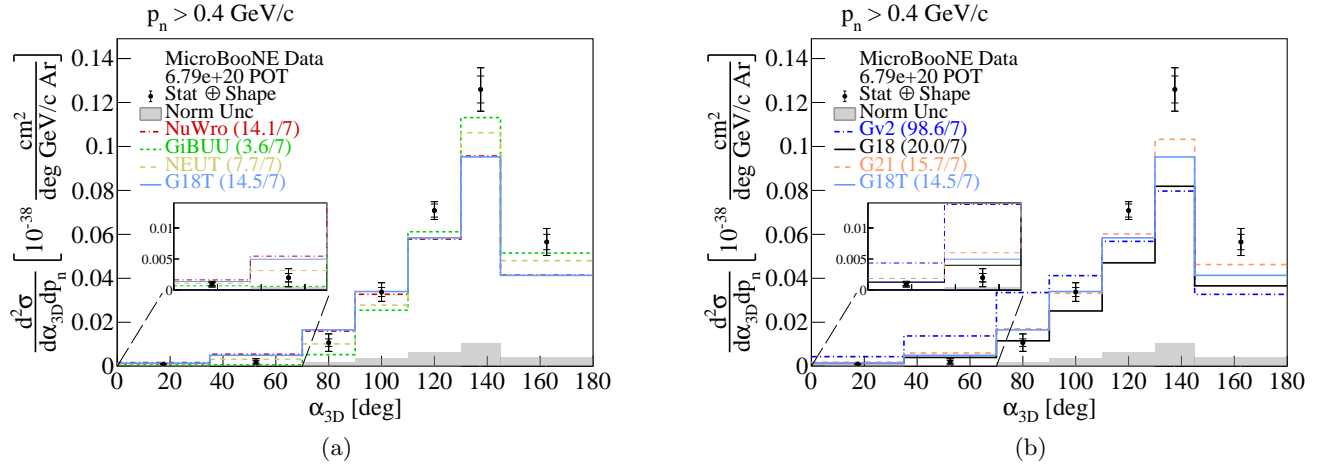


FIG. 26. The flux-integrated double-differential cross sections as a function of α_{3D} for $p_n > 0.4$ GeV/c with (a) Generator and (b) GENIE configuration predictions compared to data. Inner and outer error bars show the statistical and total (statistical and shape systematic) uncertainty at the 1σ , or 68%, confidence level. The gray band shows the normalization systematic uncertainty. The numbers in parentheses give the χ^2/ndf calculation for each one of the predictions.

A simultaneous extraction of the double-differential results across all parts of the available phase-space is presented in the Supplemental Material.

V. CONCLUSIONS

We report measurements of flux-integrated differential cross sections for event topologies with a single muon and a single proton in the final state using the Booster Neutrino Beam at Fermi National Accelerator Laboratory. The data are recorded with the MicroBooNE detector and studied for the first time in the form of single- and double-differential cross sections in novel generalized kinematic imbalance variables that consider not only the transverse, but also the longitudinal component of the missing momentum. These generalized kinematic imbalance variables show sensitivity to nuclear effects, leading to some significant differences between generator predictions and data. Some of these differences might be originating from fact that neutrinos are scattering off heavy argon nuclei. These results, in conjunction with those on lighter targets, can provide valuable information on the evolution of nuclear effects as the

target nucleus mass number increases.

The **GENIE v2.12.10 (Gv2)** cross section predictions are systematically a poor fit to data with significant shape and normalization differences across almost all variables of interest. This is in contrast to several recent measurements (e.g., [66–69]) where **Gv2** and the more modern **GENIE v3** predictions show similar shapes across many variables that only depend on either the muon or the proton kinematics, whereas these kinematic imbalance variables also depend on correlations between the leptonic and hadronic system. **Gv2** is therefore no longer able to provide a good description of the data.

GiBUU 2021 (GiBUU) is able to describe most distributions well, with the exception of ϕ_{3D} , p_n , and $p_{n\perp}$. **GiBUU** agrees particularly well in areas of phase space where final state interactions have a very large effect, for example p_n for events with $\alpha_{3D} > 135^\circ$, whereas all of the other generators show large disagreements in those regions of phase space.

The **GENIE v3.0.6 G18_10a_02.11a** cross section predictions with the MicroBooNE-specific tuning (**G18T**), on the other hand, fit the ϕ_{3D} , p_n , and $p_{n\perp}$ data well. This contrasts with the **GENIE v3.0.6 G18_10a_02.11a** configuration without additional tuning (**G18**) which shows a systematic deficit of $\approx 20\%$. The MicroBooNE-specific tuning modifies the normalization of QE and MEC events, as well as the shape of MEC and RPA suppression, and none of the tuning relied on data that included hadron kinematics. This difference indicates that the underlying physics models in **G18** can describe the correlation between lepton and hadron kinematics, although the normalization of some components need to be adjusted to better agree with data. However, in regions of phase space sensitive to FSI, this model does not perform as well as **GiBUU**, and the tuning does not improve the agreement.

The **GENIE v3.2.0 G21_11b_00.000** configuration (**G21**) serves as an example of a **GENIE** configuration that shows good agreement with data in most variables without the need for additional tuning. **NEUT** produces similar agreement as **G21** across many distributions. However, **NEUT** provides a better description of the α_{3D} data, though a worse description of the p_n data. In regions of phase space sensitive to FSI, both of these models provide poor agreement with data. In most variables and parts of the phase space, **NuWro** results in χ^2/ndf ratios fairly higher than unity.

The reported results provide precision data in new GKI variables that are more sensitive to nuclear effects for the first time. This data could be used to benchmark and tune neutrino-nucleus interaction models, particularly the modeling of final state interactions.

VI. ACKNOWLEDGEMENTS

This document was prepared by the MicroBooNE collaboration using the resources of the Fermi National Accelerator Laboratory (Fermilab), a U.S. Department of Energy, Office of Science, HEP User Facility. Fermilab is managed by Fermi Research Alliance, LLC (FRA), acting under Contract No. DE-AC02-07CH11359. This material is based upon work supported by Laboratory Directed Research and Development (LDRD) funding from Argonne National Laboratory, provided by the Director, Office of Science, of the U.S. Department of Energy under Contract No. DE-AC02-06CH11357. MicroBooNE is supported by the following: the U.S. Department of Energy, Office of Science, Offices of High Energy Physics and Nuclear Physics; the U.S. National Science Foundation; the Swiss National Science Foundation; the Science and Technology Facilities Council (STFC), part of the United Kingdom Research and Innovation; the Royal Society (United Kingdom); the UK Research and Innovation (UKRI) Future Leaders Fellowship; and The European Union’s Horizon 2020 Marie Skłodowska-Curie Actions. Additional support for the laser calibration system and cosmic ray tagger was provided by the Albert Einstein Center for Fundamental Physics, Bern, Switzerland. We also acknowledge the contributions of technical and scientific staff to the design, construction, and operation of the MicroBooNE detector as well as the contributions of past collaborators to the development of MicroBooNE analyses, without whom this work would not have been possible. For the purpose of open access, the authors have applied a Creative Commons Attribution (CC BY) license to any Author Accepted Manuscript version arising from this submission.

-
- [1] M. Tanabashi *et al.* (Particle Data Group), Review of particle physics, [Phys. Rev. D **98**, 030001 \(2018\)](#).
 - [2] K. Abe *et al.* (T2K Collaboration), Constraint on the matter–antimatter symmetry-violating phase in neutrino oscillations, [Nature **580**, 339 \(2020\)](#).
 - [3] B. Abi *et al.* (DUNE Collaboration), Long-baseline neutrino oscillation physics potential of the DUNE experiment, [Eur. Phys. J. C **80**, 978 \(2020\)](#).
 - [4] B. Abi *et al.* (DUNE Collaboration), Prospects for beyond the Standard Model physics searches at the Deep Underground Neutrino Experiment, [Eur. Phys. J. C **81**, 322 \(2021\)](#).

- [5] B. Abi *et al.* (DUNE Collaboration), Supernova neutrino burst detection with the Deep Underground Neutrino Experiment, *Eur. Phys. J. C* **81**, 423 (2021).
- [6] K. Abe *et al.* (Hyper-Kamiokande Collaboration), Hyper-Kamiokande Design Report (2018), [arXiv:1805.04163](#).
- [7] S. Nagu, J. Singh, J. Singh, and R. Singh, Impact of cross-sectional uncertainties on DUNE sensitivity due to nuclear effects, *Nuclear Physics B* **951**, 114888 (2020).
- [8] T. Dieminger, S. Dolan, D. Sgalaberna, A. Nikolakopoulos, T. Dealtry, S. Bolognesi, L. Pickering, and A. Rubbia, Uncertainties on the ν_μ/ν_e , $\bar{\nu}_\mu/\bar{\nu}_e$ and $\nu_e/\bar{\nu}_e$ cross-section ratio from the modelling of nuclear effects and their impact on neutrino oscillation experiments (2023), [arXiv:2301.08065 \[hep-ph\]](#).
- [9] M. B. Avanzini *et al.*, Comparisons and challenges of modern neutrino-scattering experiments, *Phys. Rev. D* **105**, 092004 (2022).
- [10] L. Alvarez-Ruso and others, Nustec white paper: Status and challenges of neutrino–nucleus scattering, *Progress in Particle and Nuclear Physics* **100**, 1 (2018).
- [11] M. Betancourt *et al.*, Comparisons and challenges of modern neutrino scattering experiments (tensions2016 report), *Physics Reports* **773–774**, 1 (2018), comparisons and challenges of modern neutrino scattering experiments (TENSIONS2016 report).
- [12] K. Abe *et al.* (T2K Collaboration), First T2K measurement of transverse kinematic imbalance in the muon-neutrino charged-current single- π^+ production channel containing at least one proton, *Phys. Rev. D* **103**, 112009 (2021).
- [13] P. Abratenko *et al.* (MicroBooNE Collaboration), First double-differential measurement of kinematic imbalance in neutrino interactions with the MicroBooNE detector (2023), [arXiv:2301.03706](#).
- [14] P. Abratenko *et al.* (MicroBooNE Collaboration), Multi-Differential Cross Section Measurements of Muon-Neutrino-Argon Quasielastic-like Reactions with the MicroBooNE Detector (2023), [arXiv:2301.03700](#).
- [15] R. Acciarri *et al.* (MicroBooNE Collaboration), Design and Construction of the MicroBooNE Detector, *J. Instrum.* **12** (02), P02017.
- [16] A. Aguilar-Arevalo *et al.* (MiniBooNE Collaboration), The Neutrino Flux prediction at MiniBooNE, *Phys. Rev. D* **79**, 072002 (2009).
- [17] X.-G. Lu *et al.*, Measurement of nuclear effects in neutrino interactions with minimal dependence on neutrino energy, *Phys. Rev. C* **94**, 015503 (2016).
- [18] X.-G. Lu *et al.* (MINERvA Collaboration), Measurement of final-state correlations in neutrino muon-proton mesonless production on hydrocarbon at $\langle E_\nu \rangle = 3$ GeV, *Phys. Rev. Lett.* **121**, 022504 (2018).
- [19] T. Cai *et al.* (MINERvA Collaboration), Nucleon binding energy and transverse momentum imbalance in neutrino-nucleus reactions, *Phys. Rev. D* **101**, 092001 (2020).
- [20] L. Bathe-Peters, S. Gardiner, and R. Guenette, Comparing generator predictions of transverse kinematic imbalance in neutrino-argon scattering (2022), [arXiv:2201.04664](#).
- [21] K. Abe *et al.* (T2K Collaboration), Characterization of nuclear effects in muon-neutrino scattering on hydrocarbon with a measurement of final-state kinematics and correlations in charged-current pionless interactions at T2K, *Phys. Rev. D* **98**, 032003 (2018).
- [22] D. Cplowe *et al.* (MINERvA Collaboration), Probing nuclear effects with neutrino-induced charged-current neutral pion production, *Phys. Rev. D* **102**, 072007 (2020).
- [23] A. P. Furmanski and J. T. Sobczyk, Neutrino energy reconstruction from one-muon and one-proton events, *Phys. Rev. C* **95**, 065501 (2017).
- [24] X. Lu and J. T. Sobczyk, Identification of nuclear effects in neutrino and antineutrino interactions on nuclei using generalized final-state correlations, *Phys. Rev. C* **99**, 055504 (2019).
- [25] X. Lu, Neutrino Shadow Play-Kinematic determination of nuclear effects at MINERvA, <https://minerva-docdb.fnal.gov/cgi-bin/sso/ShowDocument?docid=17864> (2018).
- [26] R. Gran *et al.* (K2K Collaboration), Measurement of the quasielastic axial vector mass in neutrino interactions on oxygen, *Phys. Rev. D* **74**, 052002 (2006).
- [27] A. Bodek and T. Cai, Removal energies and final state interaction in lepton nucleus scattering, *Eur. Phys. J. C* **79**, 293 (2019).
- [28] B. Bourguille, J. Nieves, and F. Sánchez, Inclusive and exclusive neutrino-nucleus cross sections and the reconstruction of the interaction kinematics, *J. High Energy Phys.* **2021**, 153.
- [29] P. Abratenko *et al.* (MicroBooNE Collaboration), New CC0 π genie model tune for microboone, *Phys. Rev. D* **105**, 072001 (2022).
- [30] P. Stowell, C. Wret, C. Wilkinson, L. Pickering, S. Cartwright, Y. Hayato, K. Mahn, K. McFarland, J. Sobczyk, R. Terri, L. Thompson, M. Wascko, and Y. Uchida, NUISANCE: a neutrino cross-section generator tuning and comparison framework, *J. Instrum.* **12** (01), P01016.
- [31] C. Andreopoulos *et al.*, The GENIE Neutrino Monte Carlo Generator, *Nucl. Instrum. Meth. A* **614**, 87 (2010).
- [32] C. Andreopoulos *et al.*, The GENIE Neutrino Monte Carlo Generator: Physics and User Manual (2015), [arXiv:1510.05494](#).
- [33] L. Alvarez-Ruso *et al.* (GENIE Collaboration), Recent highlights from GENIE v3, *Eur. Phys. J. ST* **230**, 4449 (2021).
- [34] U. Mosel, Neutrino event generators: foundation, status and future, *Phys. Rev. G* **46**, 113001 (2019).
- [35] T. Golan *et al.*, NuWro: the Wroclaw Monte Carlo Generator of Neutrino Interactions, *Nucl. Phys. Proc. Suppl.* **499**, 229 (2012).
- [36] Y. Hayato, A neutrino interaction simulation program library NEUT, *Acta Phys. Polon.* **B40**, 2477 (2009).
- [37] P. Abratenko *et al.* (MicroBooNE Collaboration), First measurement of differential charged current quasielasticlike ν_μ -argon scattering cross sections with the microboone detector, *Phys. Rev. Lett.* **125**, 201803 (2020).

- [38] P. Abratenko *et al.* (MicroBooNE Collaboration), Measurement of differential cross sections for ν_μ -ar charged-current interactions with protons and no pions in the final state with the microboone detector, *Phys. Rev. D* **102**, 112013 (2020).
- [39] C. Llewellyn Smith, Neutrino Reactions at Accelerator Energies, *Phys. Rept.* **3**, 261 (1972).
- [40] T. Katori, Meson Exchange Current (MEC) Models in Neutrino Interaction Generators, *AIP Conf. Proc.* **1663**, 030001 (2015).
- [41] D. Rein and L. Sehgal, Neutrino Excitation of Baryon Resonances and Single Pion Production, *Annals Phys.* **133**, 79 (1981).
- [42] U. K. Yang and A. Bodek, Parton distributions, d/u , and higher twist effects at high x , *Phys. Rev. Lett.* **82**, 2467 (1999).
- [43] T. Sjostrand, S. Mrenna, and P. Z. Skands, PYTHIA 6.4 Physics and Manual, *J. High Energ. Phys.* **2006** (05), 026.
- [44] S. Mashnik, A. Sierk, K. Gudima, and M. Baznat, CEM03 and LAQGSM03: New modeling tools for nuclear applications, *J. Phys. Conf. Ser.* **41**, 340 (2006).
- [45] R. Carrasco and E. Oset, Interaction of Real Photons With Nuclei From 100-MeV to 500-MeV, *Nucl. Phys. A* **536**, 445 (1992).
- [46] J. Nieves, F. Sanchez, I. Ruiz Simo, and M. Vicente Vacas, Neutrino Energy Reconstruction and the Shape of the CCQE-like Total Cross Section, *Phys. Rev. D* **85**, 113008 (2012).
- [47] J. Engel, Approximate treatment of lepton distortion in charged current neutrino scattering from nuclei, *Phys. Rev. C* **57**, 2004 (1998).
- [48] J. Nieves, J. E. Amaro, and M. Valverde, Inclusive quasielastic charged-current neutrino-nucleus reactions, *Phys. Rev. C* **70**, 055503 (2004).
- [49] J. Schwehr, D. Cherdack, and R. Gran, GENIE implementation of IFIC Valencia model for QE-like 2p2h neutrino-nucleus cross section (2016), [arXiv:1601.02038](https://arxiv.org/abs/1601.02038).
- [50] C. Berger and L. Sehgal, Lepton mass effects in single pion production by neutrinos, *Phys. Rev. D* **76**, 113004 (2007).
- [51] J. Tena-Vidal *et al.* (GENIE Collaboration), Neutrino-nucleon cross-section model tuning in genie v3, *Phys. Rev. D* **104**, 072009 (2021).
- [52] C. Berger and L. Sehgal, PCAC and coherent pion production by low energy neutrinos, *Phys. Rev. D* **79**, 053003 (2009).
- [53] D. Ashery, I. Navon, G. Azuelos, H. Walter, H. Pfeiffer, and F. Schlepütz, True Absorption and Scattering of Pions on Nuclei, *Phys. Rev. C* **23**, 2173 (1981).
- [54] S. Dolan, G. D. Megias, and S. Bolognesi, Implementation of the susav2-meson exchange current 1p1h and 2p2h models in genie and analysis of nuclear effects in T2K measurements, *Phys. Rev. D* **101**, 033003 (2020).
- [55] S. Dytman, Y. Hayato, R. Raboanary, J. T. Sobczyk, J. Tena-Vidal, and N. Vololonaiaina, Comparison of validation methods of simulations for final state interactions in hadron production experiments, *Phys. Rev. D* **104**, 053006 (2021).
- [56] T. Leitner, L. Alvarez-Ruso, and U. Mosel, Charged current neutrino nucleus interactions at intermediate energies, *Phys. Rev. C* **73**, 065502 (2006).
- [57] J. Nieves, I. R. Simo, and M. J. V. Vacas, Inclusive charged-current neutrino-nucleus reactions, *Phys. Rev. C* **83**, 045501 (2011).
- [58] K. M. Graczyk and J. T. Sobczyk, Form Factors in the Quark Resonance Model, *Phys. Rev. D* **77**, 053001 (2008), [Erratum: *Phys. Rev. D* **79**, 079903 (2009)].
- [59] Y. Hayato and L. Pickering, The NEUT neutrino interaction simulation program library, *Eur. Phys. J. ST* **230**, 4469 (2021).
- [60] P. S. Auchincloss *et al.*, Measurement of the inclusive charged-current cross section for neutrino and antineutrino scattering on isoscalar nucleons, *Zeitschrift für Physik C Particles and Fields* **1007**, 1431 (1990).
- [61] R. Acciari *et al.* (MicroBooNE Collaboration), The pandora multi-algorithm approach to automated pattern recognition of cosmic-ray muon and neutrino events in the microboone detector, *Eur. Phys. J. C* , 82 (2018).
- [62] S. Agostinelli *et al.* (GEANT4), GEANT4—a simulation toolkit, *Nucl. Instrum. Meth. A* **506**, 250 (2003).
- [63] P. Abratenko *et al.* (MicroBooNE Collaboration), Novel approach for evaluating detector-related uncertainties in a lartpc using microboone data, *Eur. Phys. J. C* , 454 (2022).
- [64] W. Tang, X. Li, X. Qian, H. Wei, and C. Zhang, Data unfolding with wiener-svd method, *J. Instrum.* **12** (10), P10002-P10002.
- [65] K. Mahn, *A search for muon neutrino and antineutrino disappearance in the Booster Neutrino Beam*, Ph.D. thesis, Columbia University (2009).
- [66] K. Abe *et al.*, Measurement of the charged-current electron (anti-)neutrino inclusive cross-sections at the t2k off-axis near detector, *J. High Energ. Phys.* **2020**, 114 (2020).
- [67] P. Abratenko *et al.* (MicroBooNE Collaboration), First measurement of inclusive muon neutrino charged current differential cross sections on argon at $E_\nu \sim 0.8$ GeV with the microboone detector, *Phys. Rev. Lett.* **123**, 131801 (2019).
- [68] A. Filkins *et al.* (MINERvA Collaboration), Double-differential inclusive charged-current ν_μ cross sections on hydrocarbon in minerva at $\langle E_\nu \rangle \sim 3.5$ GeV, *Phys. Rev. D* **101**, 112007 (2020).
- [69] C. L. McGivern *et al.* (MINERvA Collaboration), Cross sections for ν_μ and $\bar{\nu}_\mu$ induced pion production on hydrocarbon in the few-GeV region using MINERvA, *Phys. Rev. D* **94**, 052005 (2016).

Measurement of Nuclear Effects in neutrino-argon interactions using Generalised Kinematic
Imbalance Variables with the MicroBooNE Detector
(Dated: May 20, 2024)

I. DATA RELEASE

Overflow (underflow) values are included in the last (first) bin. The additional smearing matrix A_C should first be applied to the event distribution of an independent theoretical prediction when a comparison is performed to the data reported, and then divided by the bin width. The A_C matrices are dimensionless. The double-differential cross sections include correlations between the phase-space slices. The data release with the data results, the covariance matrices, and the additional smearing matrices is included in the DataRelease.root file. These are also included in the Supplemental Material in Sec. I, Sec. VII, and Sec. VIII, respectively. Instructions on how to use the data release and the description of the binning scheme are included in the README file.

| Cross Section p_n , Allevants | | | | |
|---------------------------------|------------------|-------------------|--|--|
| Bin # | Low edge [GeV/c] | High edge [GeV/c] | Cross Section [$10^{-38} \frac{\text{cm}^2}{(\text{GeV}/c)^{40} \text{Ar}}$] | Uncertainty [$10^{-38} \frac{\text{cm}^2}{(\text{GeV}/c)^{40} \text{Ar}}$] |
| 1 | 0 | 0.07 | 6.4406 | 1.1679 |
| 2 | 0.07 | 0.14 | 21.314 | 2.2968 |
| 3 | 0.14 | 0.2 | 36.266 | 3.6505 |
| 4 | 0.2 | 0.3 | 27.206 | 2.6118 |
| 5 | 0.3 | 0.4 | 15.223 | 2.2399 |
| 6 | 0.4 | 0.47 | 12.758 | 2.6894 |
| 7 | 0.47 | 0.55 | 9.1936 | 2.3617 |
| 8 | 0.55 | 0.65 | 6.3845 | 1.4767 |
| 9 | 0.65 | 0.75 | 4.0277 | 0.99182 |
| 10 | 0.75 | 0.85 | 3.5047 | 1.0892 |

TABLE I. Single differential cross section measurement as a function of p_n .

| Cross Section α_{3D} , All events | | | | |
|--|----------------|-----------------|--|--|
| Bin # | Low edge [deg] | High edge [deg] | Cross Section [$10^{-38} \frac{\text{cm}^2}{(\text{deg})^{40} \text{Ar}}$] | Uncertainty [$10^{-38} \frac{\text{cm}^2}{(\text{deg})^{40} \text{Ar}}$] |
| 1 | 0 | 25 | 0.0092428 | 0.0026782 |
| 2 | 25 | 50 | 0.028455 | 0.0037331 |
| 3 | 50 | 70 | 0.046157 | 0.0061733 |
| 4 | 70 | 90 | 0.064527 | 0.0091935 |
| 5 | 90 | 110 | 0.099771 | 0.011189 |
| 6 | 110 | 130 | 0.1413 | 0.014805 |
| 7 | 130 | 150 | 0.13613 | 0.015257 |
| 8 | 150 | 180 | 0.05499 | 0.0088809 |

TABLE II. Single differential cross section measurement as a function of α_{3D} .

| Cross Section φ_{3D} , All events | | | | |
|---|----------------|-----------------|--|--|
| Bin # | Low edge [deg] | High edge [deg] | Cross Section [$10^{-38} \frac{\text{cm}^2}{(\text{deg})^{40} \text{Ar}}$] | Uncertainty [$10^{-38} \frac{\text{cm}^2}{(\text{deg})^{40} \text{Ar}}$] |
| 1 | 0 | 12.5 | 0.29579 | 0.029271 |
| 2 | 12.5 | 25 | 0.2562 | 0.023545 |
| 3 | 25 | 37.5 | 0.14256 | 0.016022 |
| 4 | 37.5 | 50 | 0.09325 | 0.014113 |
| 5 | 50 | 60 | 0.076748 | 0.013939 |
| 6 | 60 | 75 | 0.045579 | 0.0089236 |
| 7 | 75 | 90 | 0.030827 | 0.0066006 |
| 8 | 90 | 106 | 0.02087 | 0.0050552 |
| 9 | 106 | 126 | 0.012219 | 0.0034782 |
| 10 | 126 | 180 | 0.0037828 | 0.0011726 |

TABLE III. Single differential cross section measurement as a function of φ_{3D} .

| Cross Section $p_{n\perp}$, All events | | | | |
|---|------------------|-------------------|--|--|
| Bin # | Low edge [GeV/c] | High edge [GeV/c] | Cross Section [$10^{-38} \frac{\text{cm}^2}{(\text{GeV}/c)^{40} \text{Ar}}$] | Uncertainty [$10^{-38} \frac{\text{cm}^2}{(\text{GeV}/c)^{40} \text{Ar}}$] |
| 1 | 0 | 0.07 | 18.062 | 2.6968 |
| 2 | 0.07 | 0.14 | 32.544 | 3.8819 |
| 3 | 0.14 | 0.2 | 36.013 | 4.2935 |
| 4 | 0.2 | 0.3 | 23.116 | 2.813 |
| 5 | 0.3 | 0.4 | 18.544 | 2.4476 |
| 6 | 0.4 | 0.47 | 11.629 | 2.0983 |
| 7 | 0.47 | 0.55 | 4.7832 | 1.4637 |
| 8 | 0.55 | 0.85 | 0.91941 | 0.34749 |

TABLE IV. Single differential cross section measurement as a function of $p_{n\perp}$.

| Cross Section $p_{n\perp,x}$, All events | | | | |
|---|------------------|-------------------|--|--|
| Bin # | Low edge [GeV/c] | High edge [GeV/c] | Cross Section [$10^{-38} \frac{\text{cm}^2}{(\text{GeV}/c)^{40} \text{Ar}}$] | Uncertainty [$10^{-38} \frac{\text{cm}^2}{(\text{GeV}/c)^{40} \text{Ar}}$] |
| 1 | -0.55 | -0.45 | 5.0018 | 1.0085 |
| 2 | -0.45 | -0.35 | 3.6489 | 0.7749 |
| 3 | -0.35 | -0.25 | 5.0634 | 1.047 |
| 4 | -0.25 | -0.15 | 11.465 | 1.4888 |
| 5 | -0.15 | -0.05 | 23.711 | 2.2797 |
| 6 | -0.05 | 0.05 | 30.292 | 2.8632 |
| 7 | 0.05 | 0.15 | 20.399 | 2.1419 |
| 8 | 0.15 | 0.25 | 8.914 | 1.2885 |
| 9 | 0.25 | 0.35 | 3.112 | 0.7141 |
| 10 | 0.35 | 0.45 | 1.422 | 0.52351 |
| 11 | 0.45 | 0.55 | 0.96175 | 0.47493 |

TABLE V. Single differential cross section measurement as a function of $p_{n\perp,x}$.

| Cross Section $p_{n\perp,y}$, All events | | | | |
|---|------------------|-------------------|--|--|
| Bin # | Low edge [GeV/c] | High edge [GeV/c] | Cross Section [$10^{-38} \frac{\text{cm}^2}{(\text{GeV}/c)^{40} \text{Ar}}$] | Uncertainty [$10^{-38} \frac{\text{cm}^2}{(\text{GeV}/c)^{40} \text{Ar}}$] |
| 1 | -0.55 | -0.45 | 0.76402 | 0.47042 |
| 2 | -0.45 | -0.35 | 2.2345 | 0.69819 |
| 3 | -0.35 | -0.25 | 4.9074 | 0.9922 |
| 4 | -0.25 | -0.15 | 10.61 | 1.419 |
| 5 | -0.15 | -0.05 | 23.149 | 2.342 |
| 6 | -0.05 | 0.05 | 32.125 | 3.2785 |
| 7 | 0.05 | 0.15 | 21.864 | 2.2828 |
| 8 | 0.15 | 0.25 | 10.255 | 1.4101 |
| 9 | 0.25 | 0.35 | 4.1982 | 0.84425 |
| 10 | 0.35 | 0.45 | 1.5029 | 0.52401 |
| 11 | 0.45 | 0.55 | 0.49323 | 0.36266 |

TABLE VI. Single differential cross section measurement as a function of $p_{n\perp,y}$.

| Cross Section $p_{n\parallel}$, All events | | | | |
|---|------------------|-------------------|--|--|
| Bin # | Low edge [GeV/c] | High edge [GeV/c] | Cross Section [$10^{-38} \frac{\text{cm}^2}{(\text{GeV}/c)^{40} \text{Ar}}$] | Uncertainty [$10^{-38} \frac{\text{cm}^2}{(\text{GeV}/c)^{40} \text{Ar}}$] |
| 1 | -0.55 | -0.45 | 7.3354 | 2.263 |
| 2 | -0.45 | -0.35 | 6.7636 | 1.4412 |
| 3 | -0.35 | -0.25 | 10.489 | 1.4262 |
| 4 | -0.25 | -0.15 | 17.696 | 1.7962 |
| 5 | -0.15 | -0.05 | 25.676 | 2.3889 |
| 6 | -0.05 | 0.05 | 26.294 | 2.6477 |
| 7 | 0.05 | 0.15 | 14.997 | 1.5763 |
| 8 | 0.15 | 0.25 | 4.3977 | 0.81678 |
| 9 | 0.25 | 0.35 | 0.26795 | 0.41179 |
| 10 | 0.35 | 0.45 | -0.22201 | 0.19504 |

TABLE VII. Single differential cross section measurement as a function of $p_{n\parallel}$.

| Cross Section p_n , $\alpha_{3D} < 45^\circ$ | | | | |
|--|------------------|-------------------|--|--|
| Bin # | Low edge [GeV/c] | High edge [GeV/c] | Cross Section [$10^{-38} \frac{\text{cm}^2}{(\text{GeV}/c)^{40} \text{Ar}}$] | Uncertainty [$10^{-38} \frac{\text{cm}^2}{(\text{GeV}/c)^{40} \text{Ar}}$] |
| 1 | 0 | 0.1 | 0.028159 | 0.0070451 |
| 2 | 0.1 | 0.2 | 0.09376 | 0.012414 |
| 3 | 0.2 | 0.3 | 0.04408 | 0.009544 |
| 4 | 0.3 | 0.4 | 0.015599 | 0.0058132 |
| 5 | 0.4 | 0.85 | 0.00083573 | 0.0008078 |

TABLE VIII. Double differential cross section measurement as a function of p_n for $\alpha_{3D} < 45^\circ$.

| Cross Section p_n , $135^\circ < \alpha_{3D} < 180^\circ$ | | | | |
|---|------------------|-------------------|--|--|
| Bin # | Low edge [GeV/c] | High edge [GeV/c] | Cross Section [$10^{-38} \frac{\text{cm}^2}{(\text{GeV}/c)^{40} \text{Ar}}$] | Uncertainty [$10^{-38} \frac{\text{cm}^2}{(\text{GeV}/c)^{40} \text{Ar}}$] |
| 1 | 0 | 0.08 | 0.0167 | 0.011364 |
| 2 | 0.08 | 0.15 | 0.08459 | 0.016098 |
| 3 | 0.15 | 0.23 | 0.12713 | 0.019017 |
| 4 | 0.23 | 0.3 | 0.14042 | 0.02328 |
| 5 | 0.3 | 0.4 | 0.098465 | 0.017631 |
| 6 | 0.4 | 0.85 | 0.068701 | 0.014215 |

TABLE IX. Double differential cross section measurement as a function of p_n for $135^\circ < \alpha_{3D} < 180^\circ$.

| Cross Section α_{3D} , $p_n < 0.2 \text{ GeV}/c$ | | | | |
|---|----------------|-----------------|--|--|
| Bin # | Low edge [deg] | High edge [deg] | Cross Section [$10^{-38} \frac{\text{cm}^2}{(\text{deg})^{40} \text{Ar}}$] | Uncertainty [$10^{-38} \frac{\text{cm}^2}{(\text{deg})^{40} \text{Ar}}$] |
| 1 | 0 | 35 | 0.053491 | 0.0071818 |
| 2 | 35 | 70 | 0.12055 | 0.012314 |
| 3 | 70 | 92 | 0.20117 | 0.019441 |
| 4 | 92 | 114 | 0.21589 | 0.021971 |
| 5 | 114 | 136 | 0.19916 | 0.017257 |
| 6 | 136 | 158 | 0.11911 | 0.012186 |
| 7 | 158 | 180 | 0.044109 | 0.0072957 |

TABLE X. Double differential cross section measurement as a function of α_{3D} for $p_n < 0.2 \text{ GeV}/c$.

| Cross Section α_{3D} , $p_n > 0.4 \text{ GeV}/c$ | | | | |
|---|----------------|-----------------|--|--|
| Bin # | Low edge [deg] | High edge [deg] | Cross Section [$10^{-38} \frac{\text{cm}^2}{(\text{deg})^{40} \text{Ar}}$] | Uncertainty [$10^{-38} \frac{\text{cm}^2}{(\text{deg})^{40} \text{Ar}}$] |
| 1 | 0 | 35 | 0.00095038 | 0.00045408 |
| 2 | 35 | 70 | 0.0019962 | 0.0015217 |
| 3 | 70 | 90 | 0.01073 | 0.0044479 |
| 4 | 90 | 110 | 0.03376 | 0.0056656 |
| 5 | 110 | 130 | 0.070846 | 0.0076066 |
| 6 | 130 | 145 | 0.12594 | 0.014246 |
| 7 | 145 | 180 | 0.056519 | 0.0072774 |

TABLE XI. Double differential cross section measurement as a function of α_{3D} for $p_n > 0.4 \text{ GeV}/c$.

II. ACCEPTANCE-REJECTION CURVES

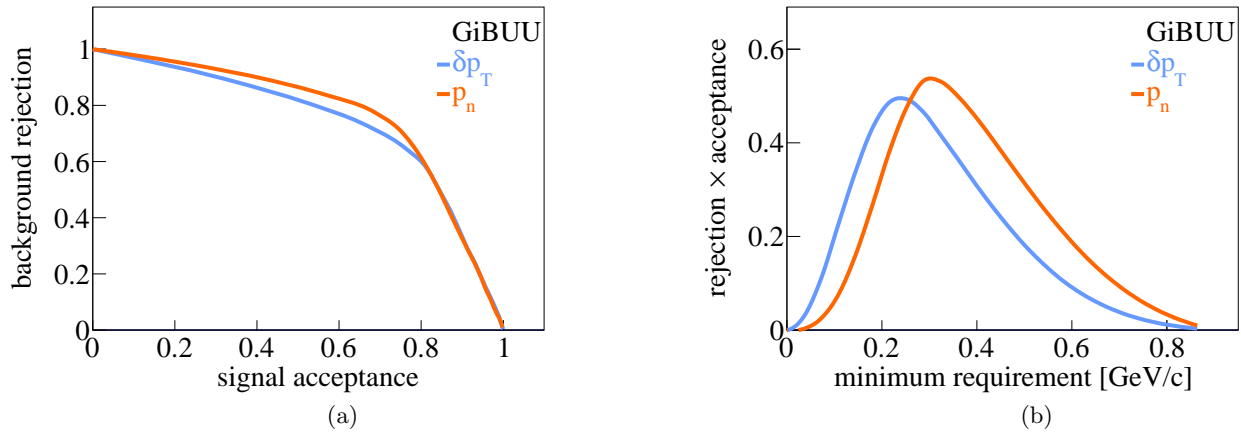


FIG. 1. (a) Signal acceptance fraction vs background rejection fraction as a function of the cut on the reconstructed missing momentum p_n (orange) and the transverse missing momentum δp_T (blue) for CC1p0 π events using the GiBUU prediction. (b) Evolution of the product between the signal acceptance and the background rejection denoted as “rejection \times acceptance” as a function of the cut value.

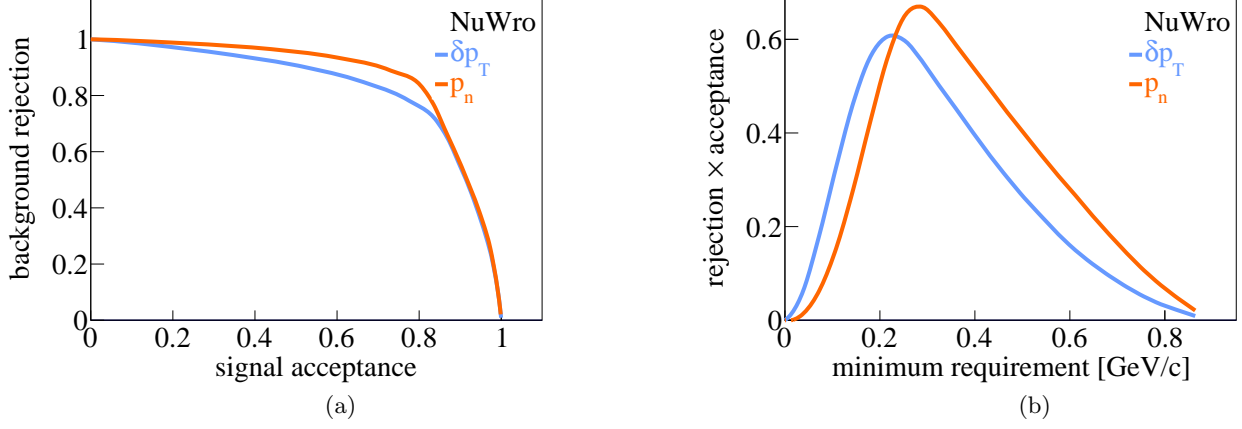


FIG. 2. (a) Signal acceptance fraction vs background rejection fraction as a function of the cut on the reconstructed missing momentum p_n (orange) and the transverse missing momentum δp_T (blue) for CC1p0 π events using the NuWro prediction. (b) Evolution of the product between the signal acceptance and the background rejection denoted as “rejection \times acceptance” as a function of the cut value.

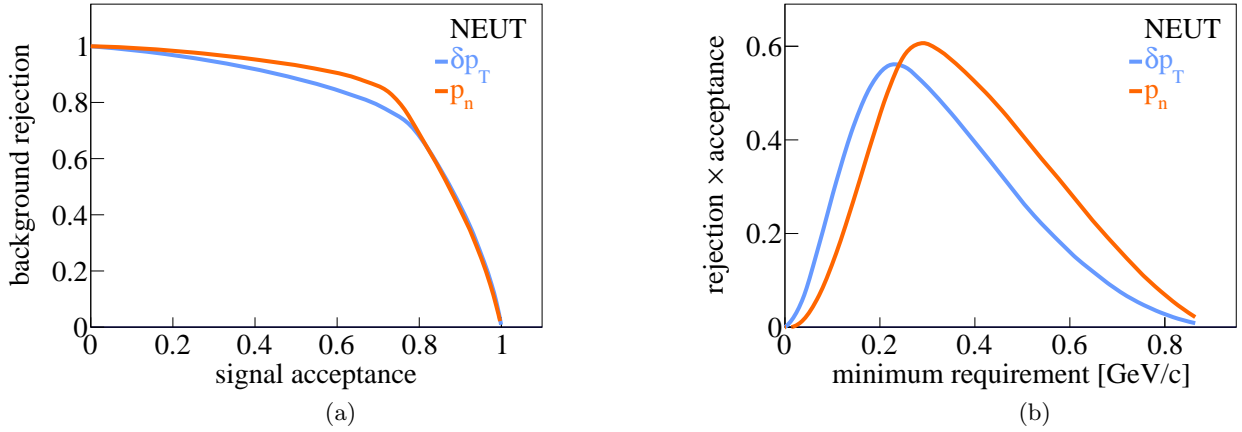


FIG. 3. (a) Signal acceptance fraction vs background rejection fraction as a function of the cut on the reconstructed missing momentum p_n (orange) and the transverse missing momentum δp_T (blue) for CC1p0 π events using the NEUT prediction. (b) Evolution of the product between the signal acceptance and the background rejection denoted as “rejection \times acceptance” as a function of the cut value.

III. GENERALIZED AND TRANSVERSE KINEMATIC IMBALANCE CROSS SECTIONS WITHOUT FSI

Both the GKI and the TKI variables are presented below in the absence of FSI effects.

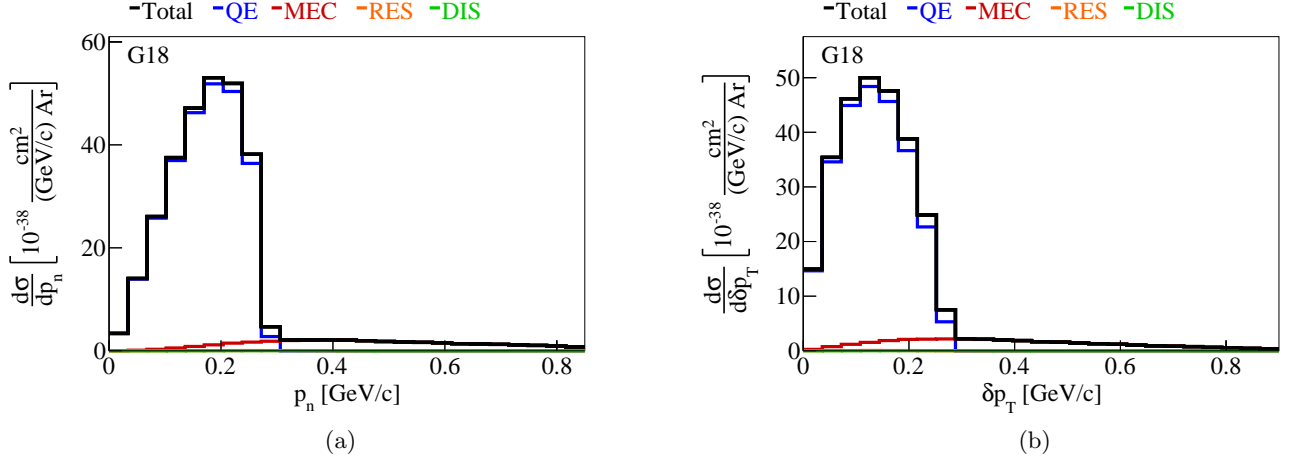


FIG. 4. The flux-integrated single-differential cross section interaction breakdown as a function of (left) p_n and (right) δp_T . Colored lines show the results of theoretical cross section calculations using the G18 prediction without FSI for QE (blue), MEC (red), RES (orange), and DIS (green) interactions.

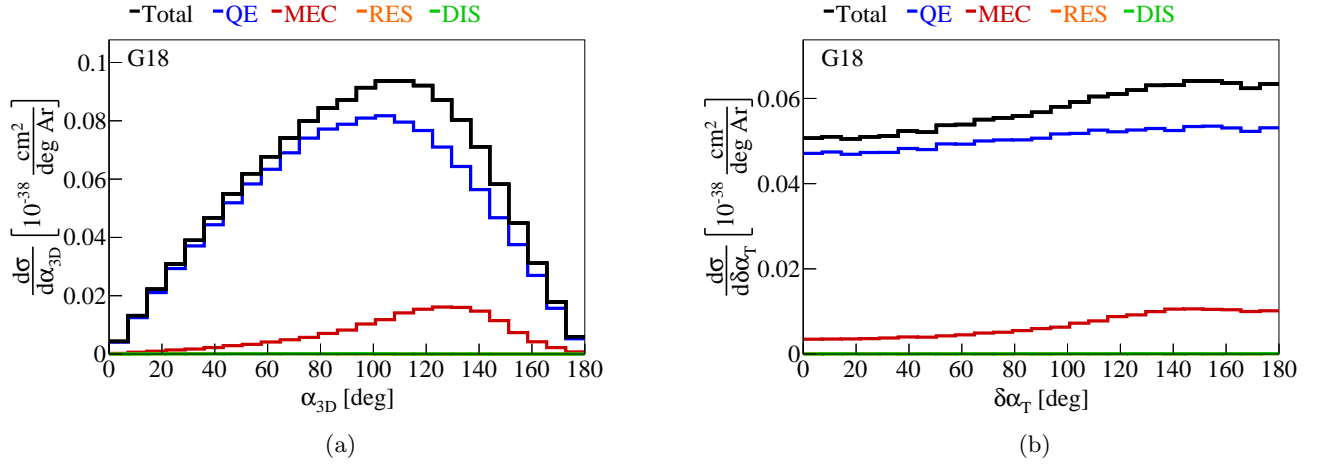


FIG. 5. The flux-integrated single-differential cross section interaction breakdown as a function of (left) α_{3D} and (right) $\delta\alpha_T$. Colored lines show the results of theoretical cross section calculations using the G18 prediction without FSI for QE (blue), MEC (red), RES (orange), and DIS (green) interactions.

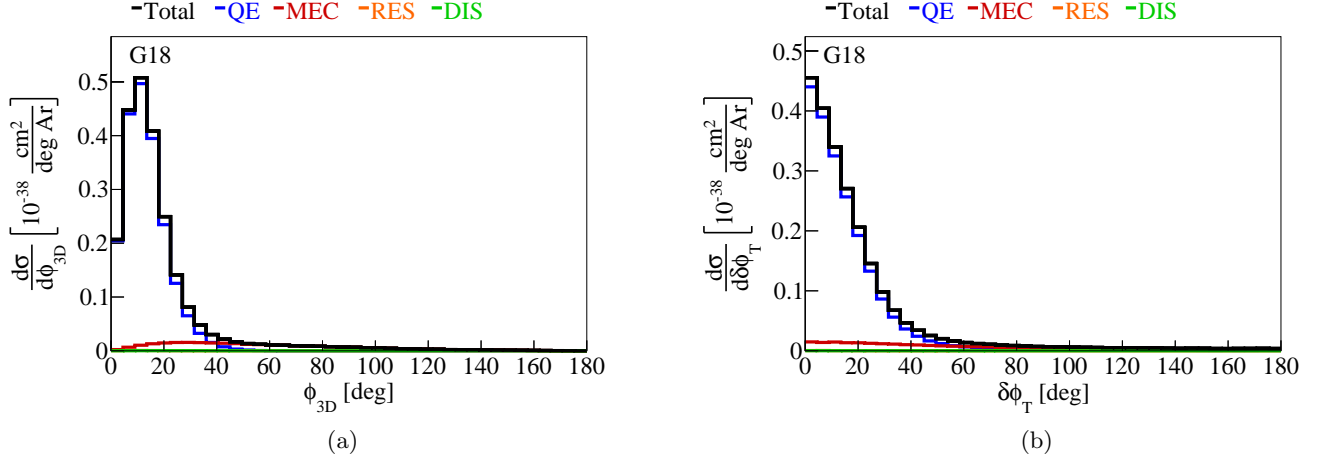


FIG. 6. The flux-integrated single-differential cross section interaction breakdown as a function of (left) ϕ_{3D} and (right) $\delta\phi_T$. Colored lines show the results of theoretical cross section calculations using the G18 prediction without FSI for QE (blue), MEC (red), RES (orange), and DIS (green) interactions.

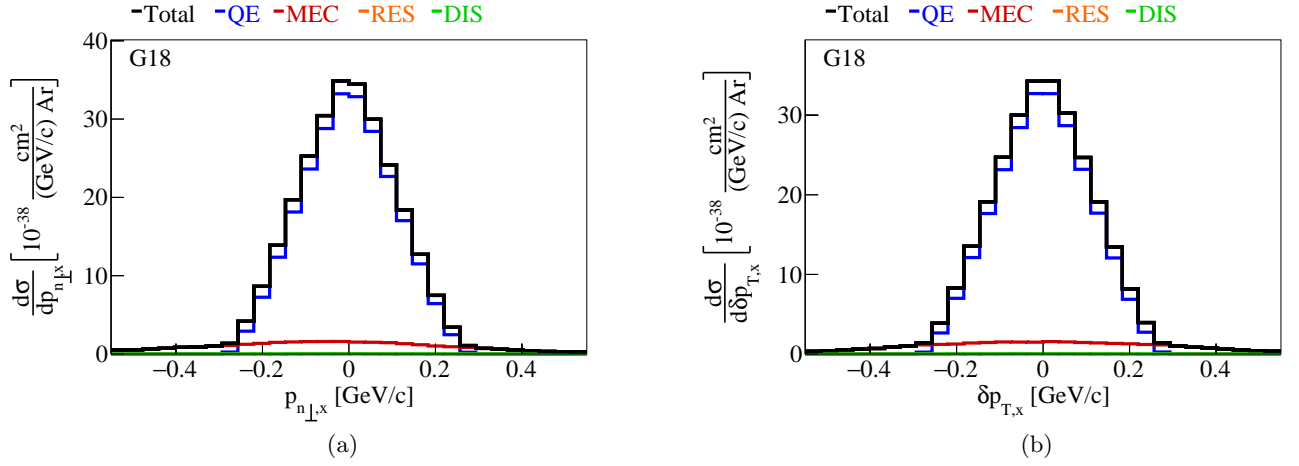


FIG. 7. The flux-integrated single-differential cross section interaction breakdown as a function of (left) $p_{n,\perp x}$ and (right) $\delta p_{T,x}$. Colored lines show the results of theoretical cross section calculations using the G18 prediction without FSI for QE (blue), MEC (red), RES (orange), and DIS (green) interactions.

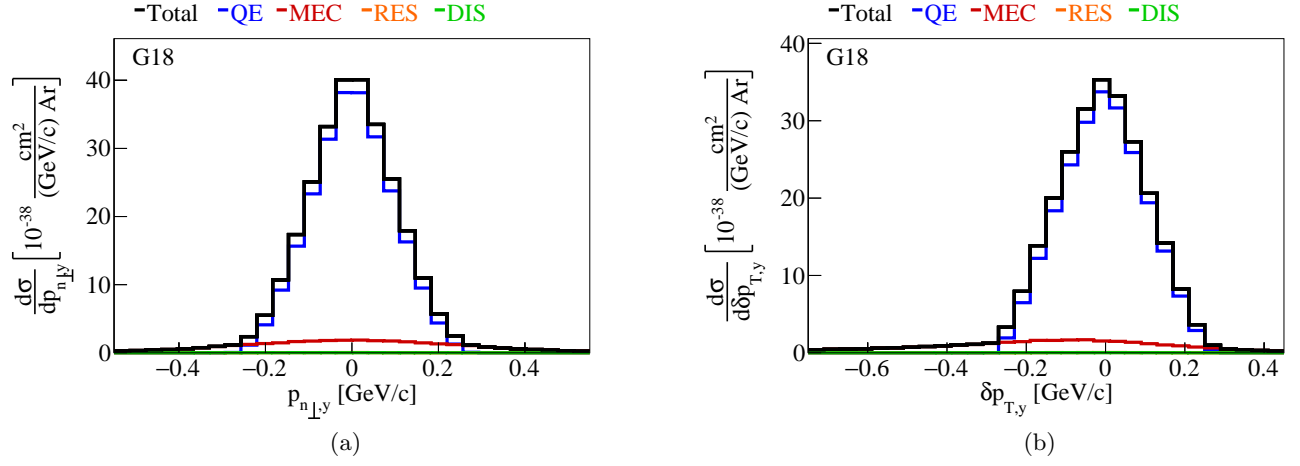


FIG. 8. The flux-integrated single-differential cross section interaction breakdown as a function of (left) $p_{n,\perp y}$ and (right) $p_{T,y}$. Colored lines show the results of theoretical cross section calculations using the G18 prediction without FSI for QE (blue), MEC (red), RES (orange), and DIS (green) interactions.

IV. TWO-DIMENSIONAL SIMULTANEOUS CROSS SECTION EXTRACTION

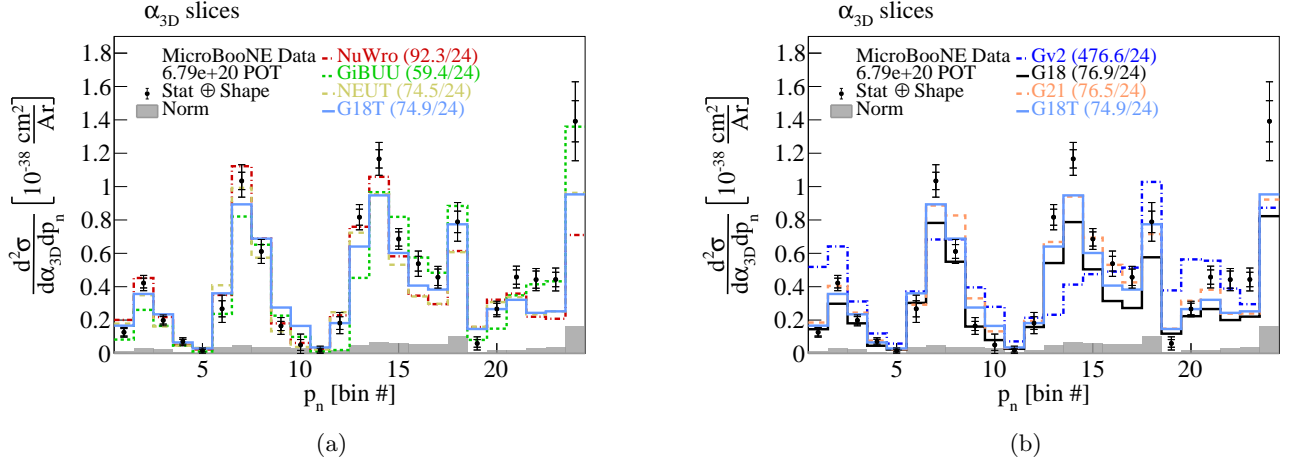


FIG. 9. The flux-integrated double-differential cross sections as a function of the p_n bin number. (Left) Generator and (right) GENIE configuration predictions are compared to data. Inner and outer error bars show the statistical and total (statistical and shape systematic) uncertainty at the 1σ , or 68%, confidence level. The gray band shows the normalization systematic uncertainty. The numbers in parentheses show the χ^2/ndf calculation for each one of the predictions.

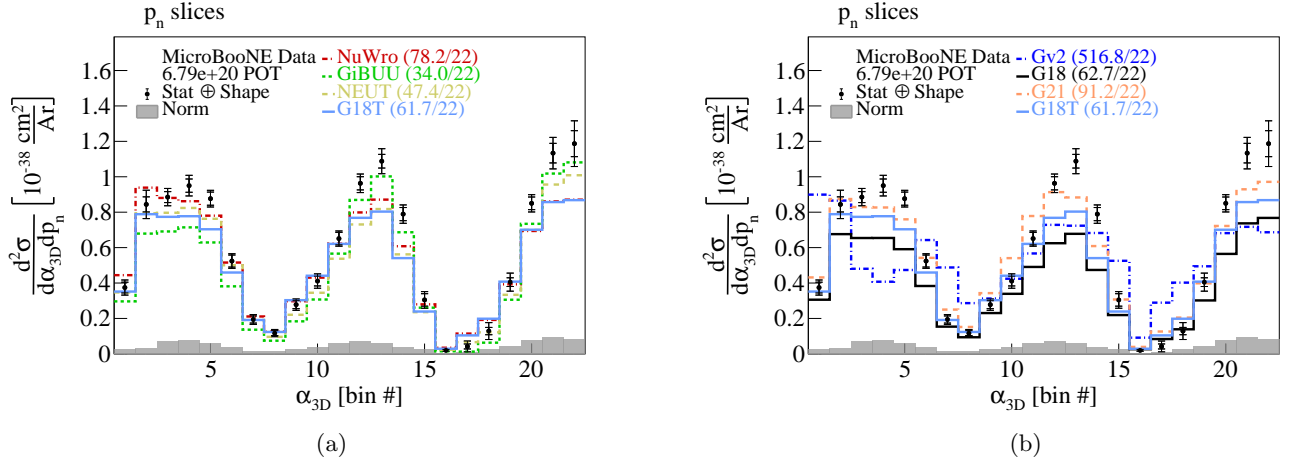


FIG. 10. The flux-integrated double-differential cross sections as a function of the $\delta\alpha_{3D}$ bin number. (Left) Generator and (right) GENIE configuration predictions are compared to data. Inner and outer error bars show the statistical and total (statistical and shape systematic) uncertainty at the 1σ , or 68%, confidence level. The gray band shows the normalization systematic uncertainty. The numbers in parentheses show the χ^2/ndf calculation for each one of the predictions.

V. FAKE DATA STUDIES

In order to ensure that the unfolded data results are not biased due to the choice of the original MC, we performed fake data studies and treated the signal reconstructed events from an alternative model as if they were real data. We investigated three samples: (a) using NuWro events, (b) by removing the weights corresponding to the MicroBooNE tune (NoTune) and, (c) by multiplying the weight for the MEC events by 2 (TwiceMEC). We then extracted the cross section from these fake data using our nominal MC response and covariance matrices and the Wiener-SVD filter both for the single- and double-differential cross sections. Given that we have the true cross section information from the fake data, we compared the fake data extracted cross section to the corresponding truth-level cross section predictions. The outcome agreed within an expected uncertainty. In the case of all these variations, uncertainties due to beam exposure, number-of-targets, detector, fluxes, and re-interactions are irrelevant and were not included in the fake-data uncertainty for comparison. Only the uncorrelated uncertainties (cross section, statistical, MC statistical, alternative generator) were used for the minimization procedure and are shown on the plots to account for the unfolding process and the change in the event generator. The combination of these uncertainties covers the differences between the unfolded fake data points (black) and the alternative-generator theory results (orange). The relevant A_C matrices have been applied to the generator predictions.

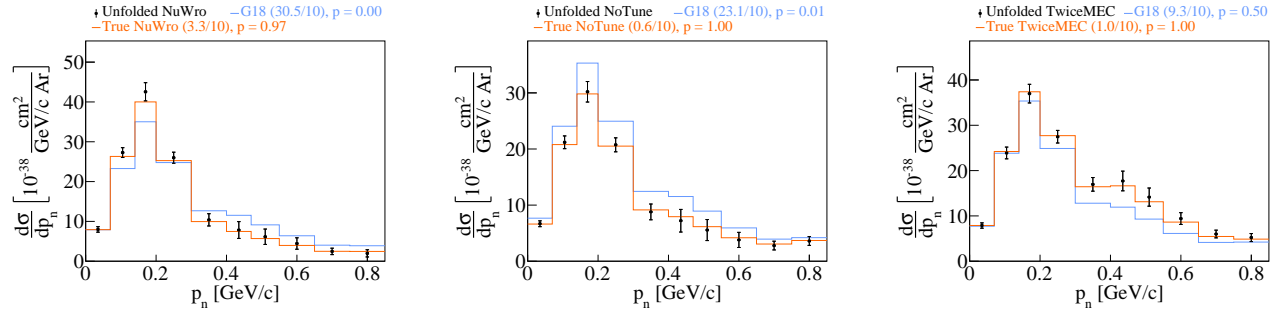


FIG. 11. Fake data studies for p_n using (left) NuWro, (center) GENIE without the MicroBooNE tune (NoTune), and (right) twice the weights for MEC events (TwiceMEC) as fake data samples.

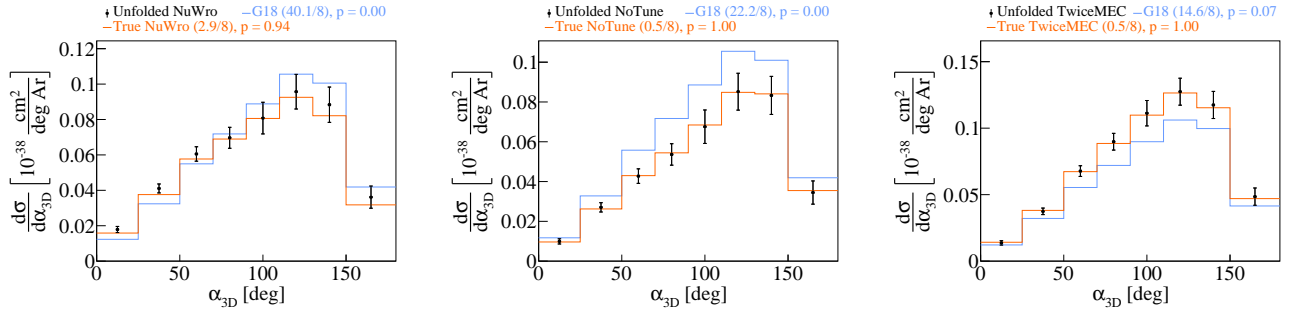


FIG. 12. Fake data studies for α_{3D} using (left) NuWro, (center) GENIE without the MicroBooNE tune (NoTune), and (right) twice the weights for MEC events (TwiceMEC) as fake data samples.

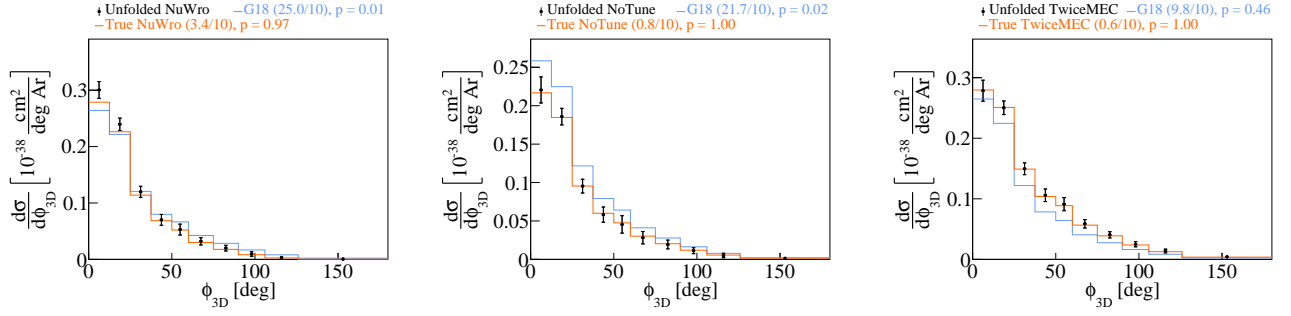


FIG. 13. Fake data studies for ϕ_{3D} using (left) NuWro, (center) GENIE without the MicroBooNE tune (NoTune), and (right) twice the weights for MEC events (TwiceMEC) as fake data samples.

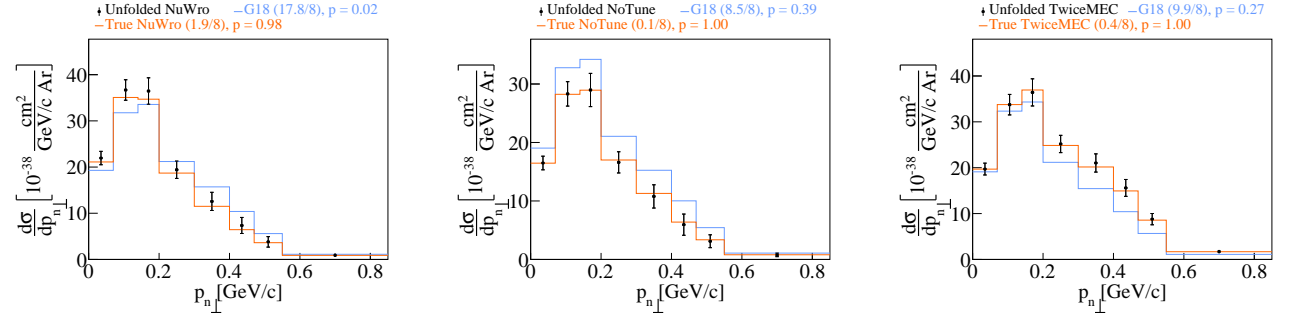


FIG. 14. Fake data studies for $p_{n\perp}$ using (left) NuWro, (center) GENIE without the MicroBooNE tune (NoTune), and (right) twice the weights for MEC events (TwiceMEC) as fake data samples.

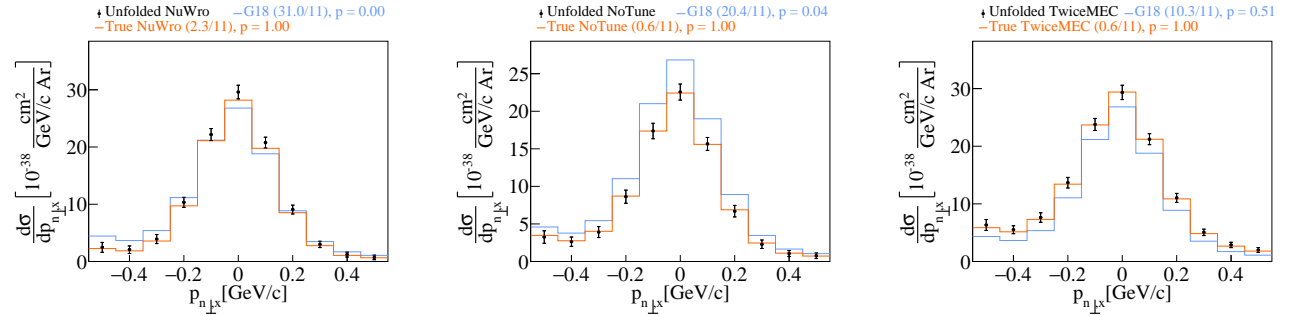


FIG. 15. Fake data studies for $p_{n\perp,x}$ using (left) NuWro, (center) GENIE without the MicroBooNE tune (NoTune), and (right) twice the weights for MEC events (TwiceMEC) as fake data samples.

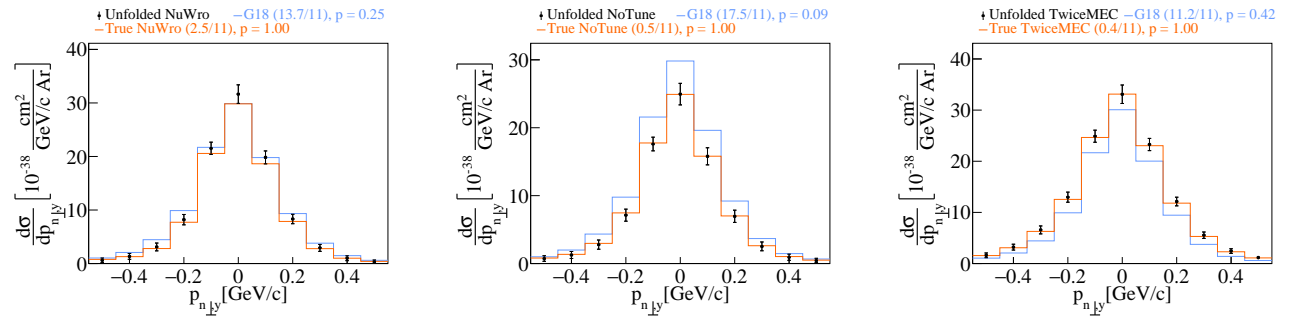


FIG. 16. Fake data studies for $p_{n\perp,y}$ using (left) NuWro, (center) GENIE without the MicroBooNE tune (NoTune), and (right) twice the weights for MEC events (TwiceMEC) as fake data samples.

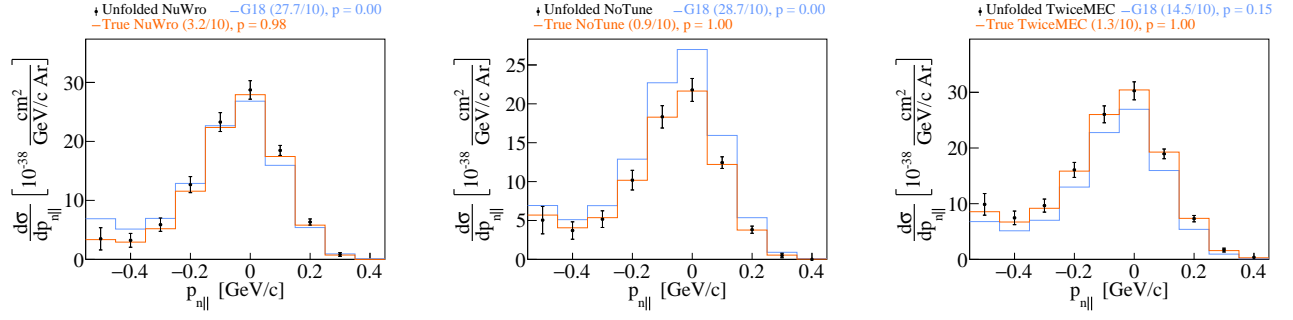


FIG. 17. Fake data studies for $p_{n||}$ using (left) NuWro, (center) GENIE without the MicroBooNE tune (NoTune), and (right) twice the weights for MEC events (TwiceMEC) as fake data samples.

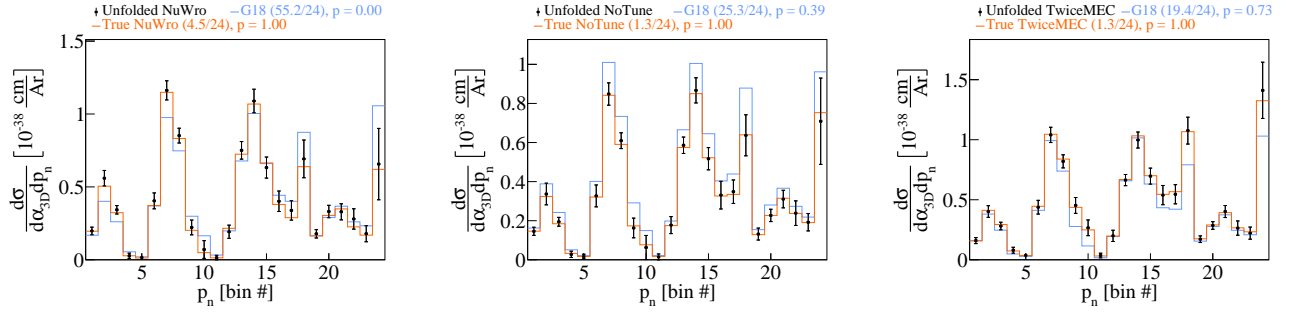


FIG. 18. Fake data studies for $p_{n||}$ in α_{3D} slices using (left) NuWro, (center) GENIE without the MicroBooNE tune (NoTune), and (right) twice the weights for MEC events (TwiceMEC) as fake data samples.

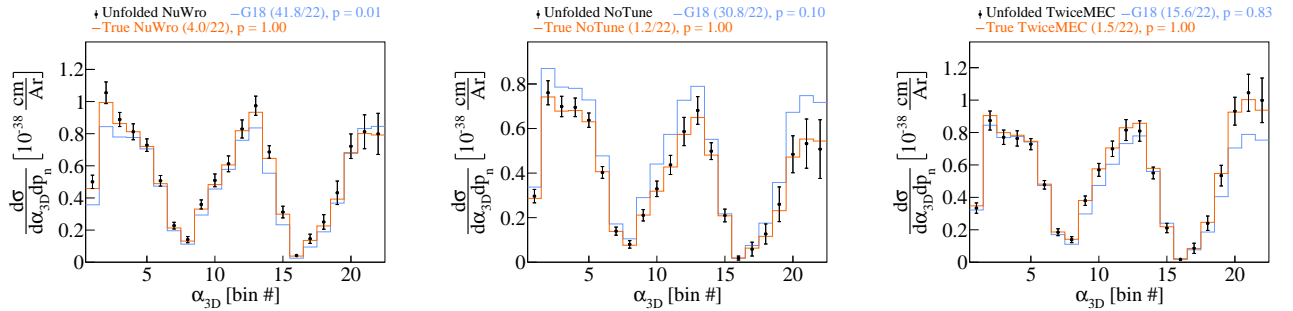


FIG. 19. Fake data studies for α_{3D} in $p_{n||}$ slices using (left) NuWro, (center) GENIE without the MicroBooNE tune (NoTune), and (right) twice the weights for MEC events (TwiceMEC) as fake data samples.

VI. MUON & PROTON EFFICIENCIES

Figure 20 shows the proton and muon efficiencies in the momenta range of interest given the CC1p0 π signal definition, namely $0.1 < p_\mu < 1.2 \text{ GeV}/c$ and $0.3 < p_p < 1 \text{ GeV}/c$. Figure 21 shows the proton and muon efficiencies as a function of $\cos\theta$, demonstrating the full angular coverage in the MicroBooNE LArTPC detector.

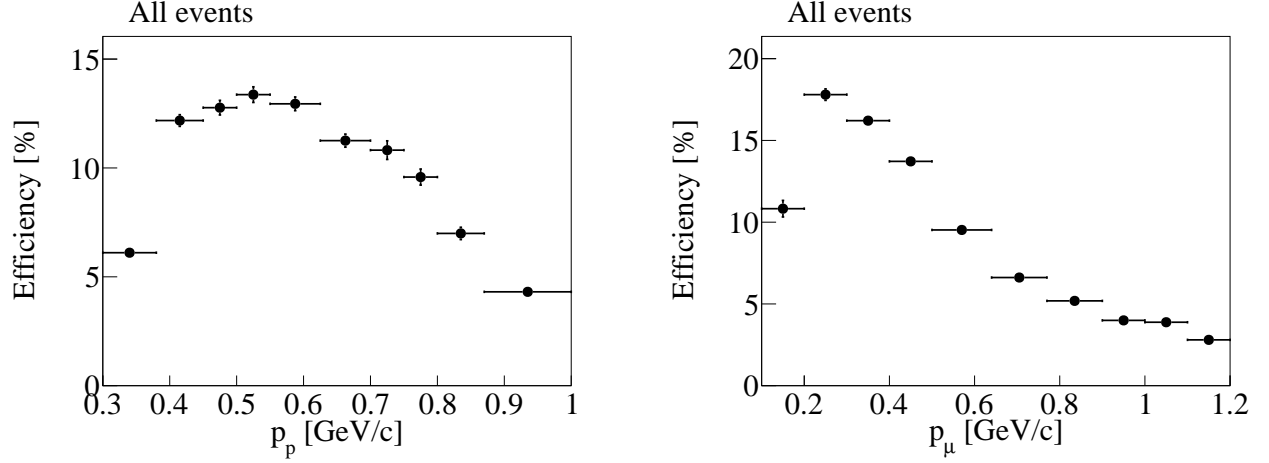


FIG. 20. Efficiency as a function of the (left) proton and (right) muon momenta.

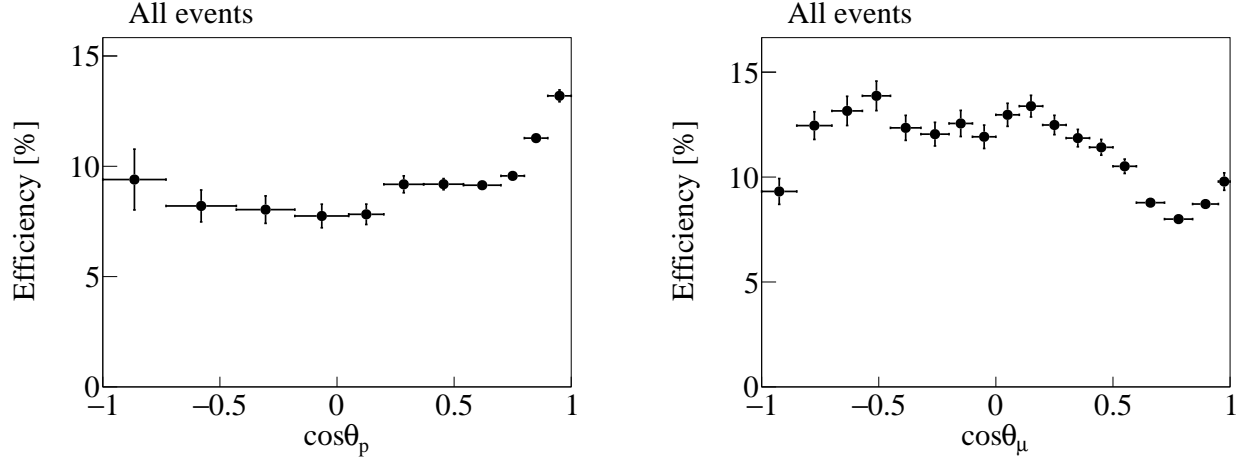


FIG. 21. Efficiency as a function of the (left) proton and (right) muon $\cos\theta$.

VII. COVARIANCE MATRICES

The figures below present the covariance matrices for the cross section results presented in this work. They are also included in the DataRelease.root file. More details on how to manipulate the covariance matrices in order to calculate a χ^2 GoF metric can be found in the README file.

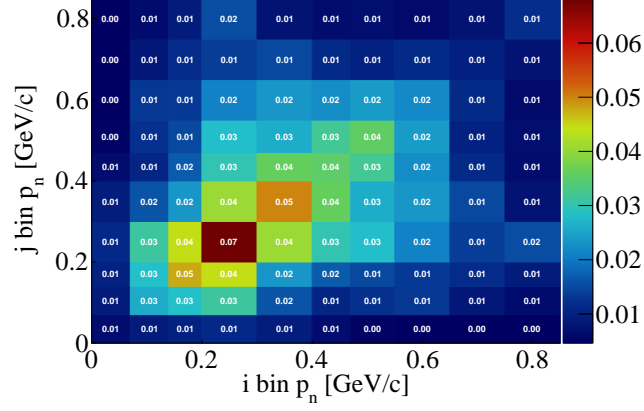


FIG. 22. Covariance matrix for p_n .

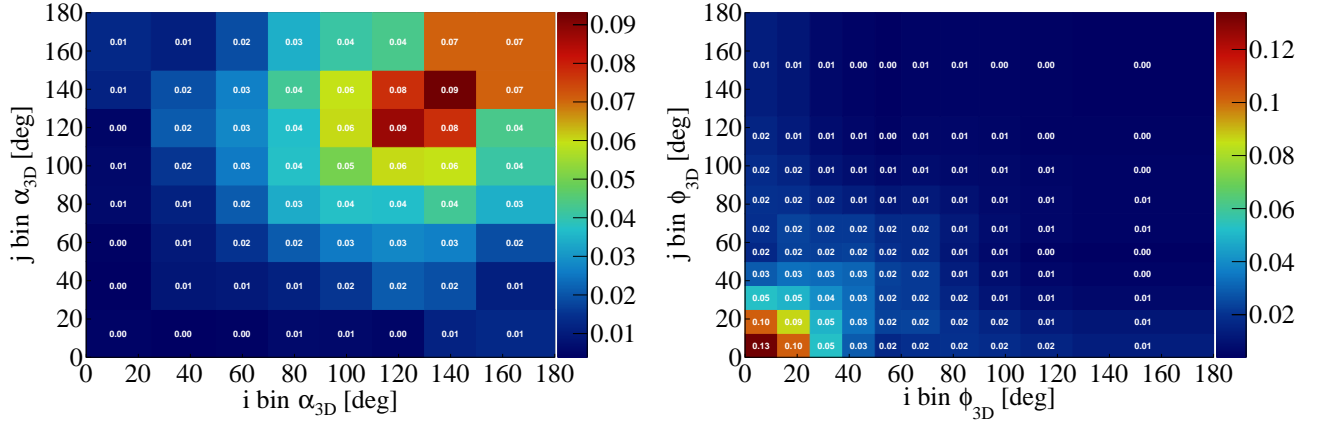
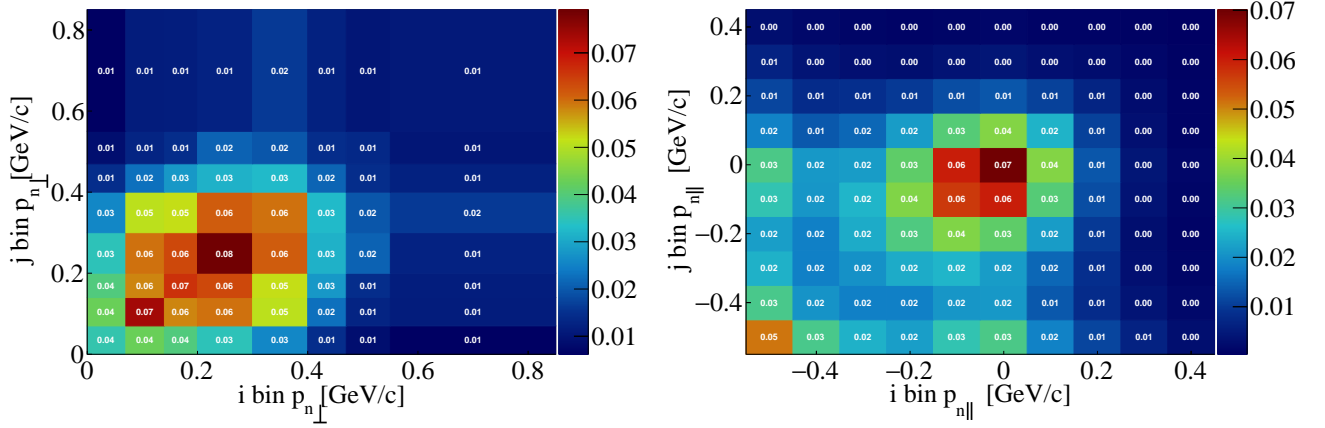
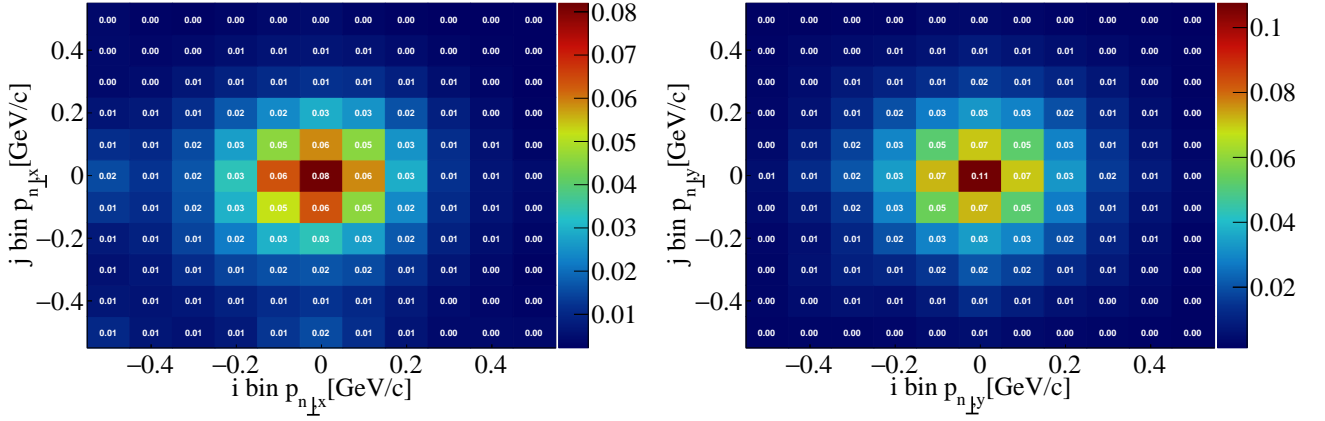
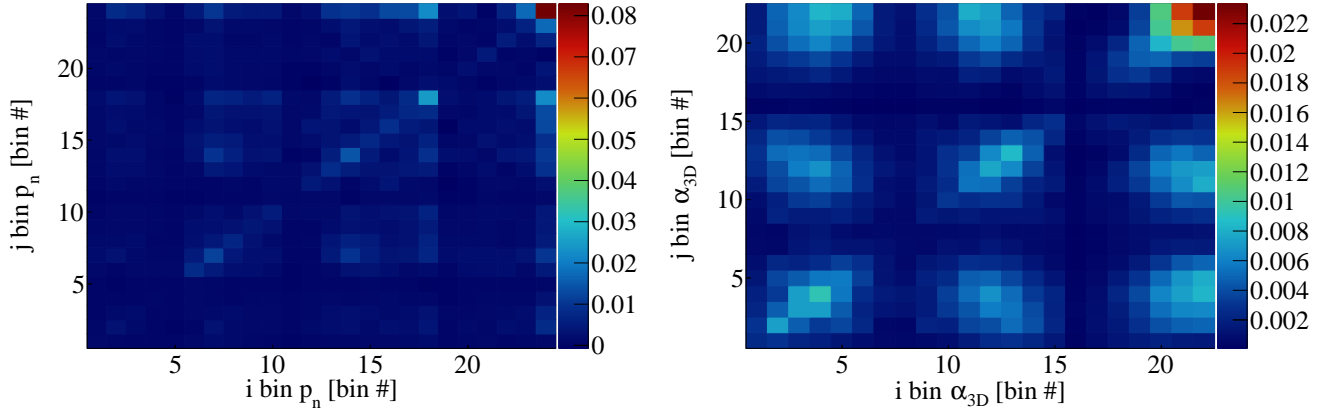


FIG. 23. Covariance matrix for (left) α_{3D} and (right) ϕ_{3D} .

FIG. 24. Covariance matrix for (left) $p_{n\perp}$ and (right) $p_{n\parallel}$.FIG. 25. Covariance matrix for (left) $p_{n\perp,x}$ and (right) $p_{n\perp,y}$.FIG. 26. Covariance matrix for (left) p_n in α_{3D} bins and (right) α_{3D} in p_n bins.

VIII. ADDITIONAL SMEARING MATRICES

The figures below present the additional smearing matrices for the cross section results presented in this work. They are also included in the DataRelease.root file.

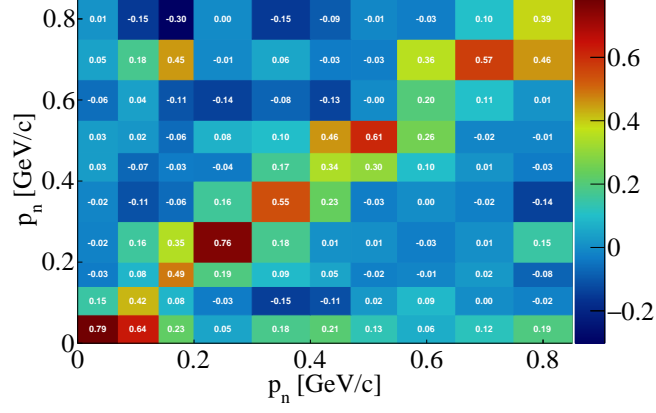


FIG. 27. Additional smearing matrix for p_n .

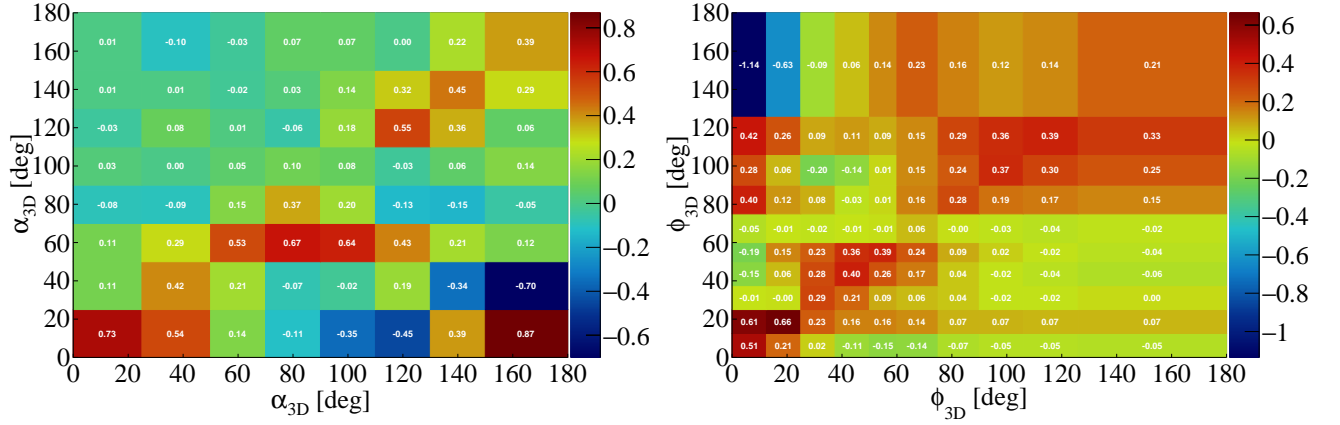
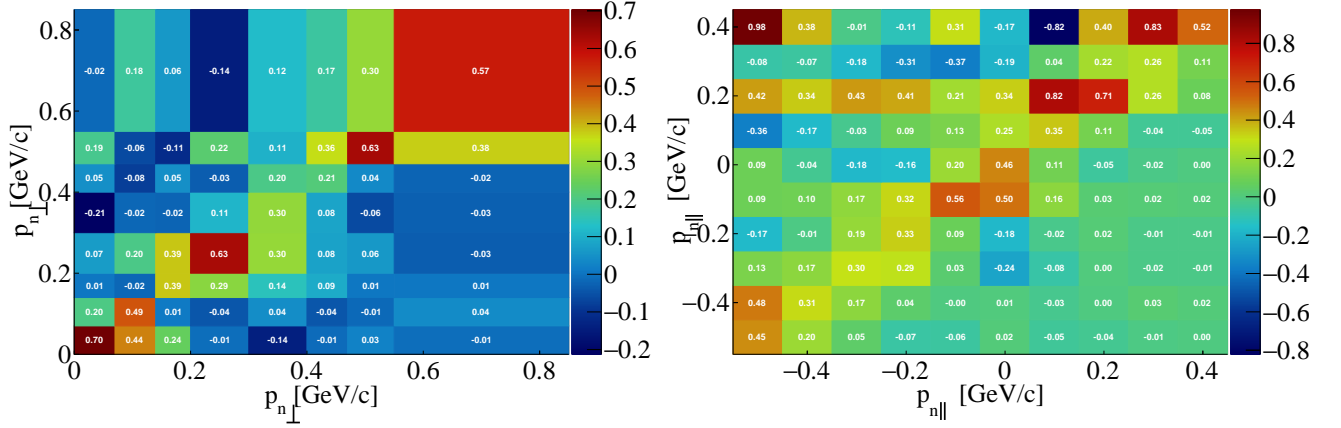
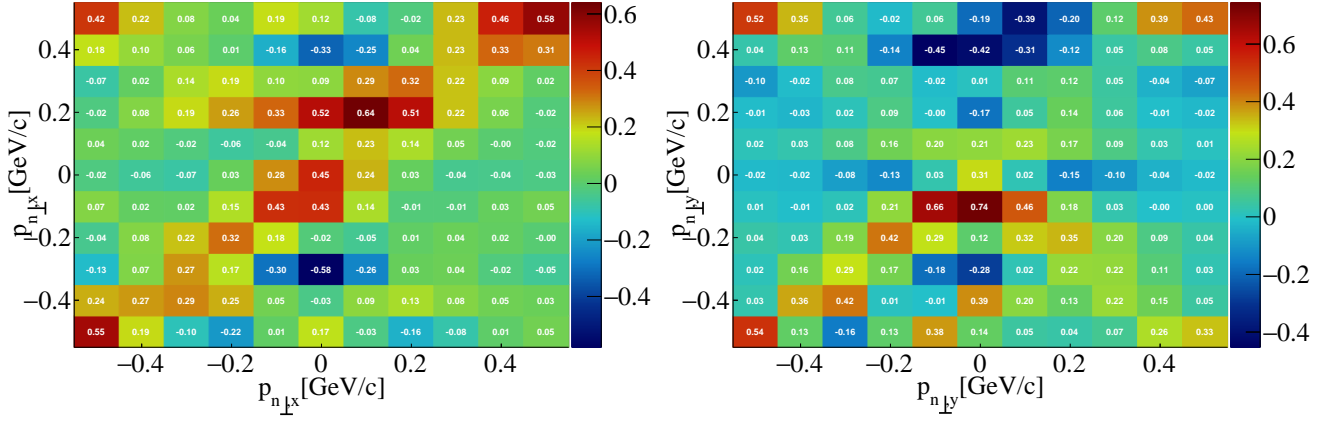
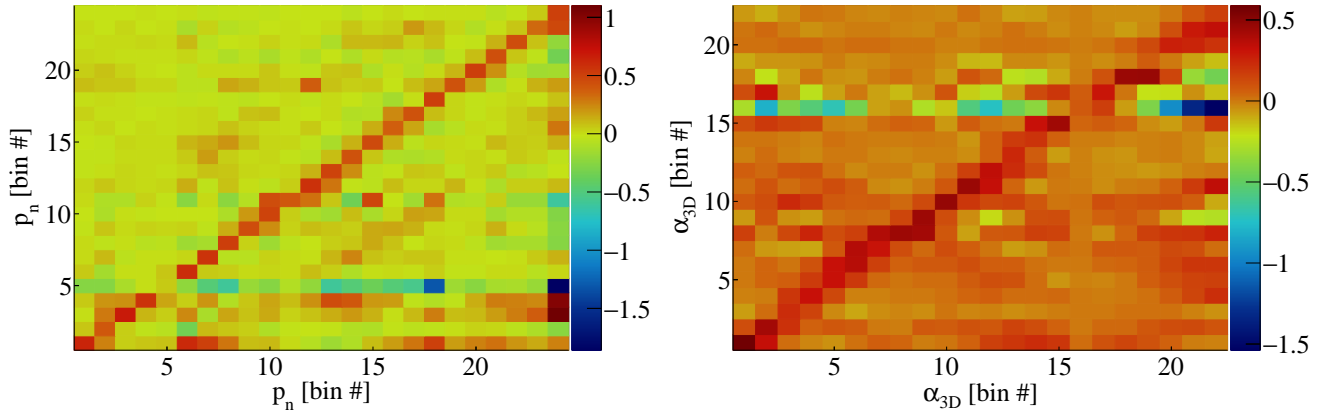


FIG. 28. Additional smearing matrix for (left) α_{3D} and (right) ϕ_{3D} .

FIG. 29. Additional smearing matrix for (left) $p_{n\perp}$ and (right) $p_{n\parallel}$.FIG. 30. Additional smearing matrix for (left) $p_{n\perp,x}$ and (right) $p_{n\perp,y}$.FIG. 31. Additional smearing matrix for (left) p_n in α_{3D} bins and (right) α_{3D} in p_n bins.